Aerodynamic performances and wake topology past a square cylinder in the interface of two different-velocity streams

R. El Mansy,[1] J.M. Bergadà,[1] Wasim Sarwar,[2] and Fernando Mellibovsky[2, a)]
[1)] *Fluid Mechanics Department, Universitat Politècnica de Catalunya, 08034, Barcelona, Spain*
[2)] *Department of Physics, Aerospace Engineering Division, Universitat Politècnica de Catalunya, 08034, Barcelona, Spain*

(Dated: 16 April 2022)

We analyse the incompressible flow past a square cylinder immersed in the wake of an upstream splitter plate which separates two streams of different velocities, U_T (top) and U_B (bottom). The Reynolds number associated to the flow below the plate is kept constant at $Re_B = DU_B/\nu = 56$, based on the square cylinder side D as characteristic length. The top-to-bottom flow dissymmetry is measured by the ratio $R \equiv Re_T/Re_B \in [1, 5.3]$ between the Reynolds numbers above and below the plate. The equivalent bulk Reynolds, taken as the mean between top and bottom changes with R in the range $Re \equiv (Re_T + Re_B)/2 \in [56, 178]$. A Hopf bifurcation occurs at $R = 2.1 \pm 0.1$ ($Re = 86.8 \pm 2.8$), which results in an asymmetric Kármán vortex street with vortices only showing on the high-velocity side of the wake. A spanwise modulational instability is responsible for the three-dimensionalisation of the flow at $R \simeq 3.1$ ($Re \simeq 115$) with associated wavelength $\lambda_z \simeq 2.4$. For velocity ratios $R \geq 4$, the flow becomes spatio-temporally chaotic. The migration of the mean stagnation and base pressure points on the front and rear surfaces of the cylinder as R is increased determine the boundary layer properties on the top and bottom surfaces and, with them, the shear layers that roll up into the formation of Kármán vortices, which in turn help clarify the evolution of the lift and drag coefficients. The symmetries of the different solutions across the flow transition regime are imprinted on the top and bottom boundary layers and can therefore be analysed from the time evolution and spanwise distribution of trailing edge boundary layer displacement thickness at the top and bottom rear corners.

I. INTRODUCTION

In many applications, bluff bodies are placed inside boundary layers or wakes and the flow around them is decisively modified by the inhomogeneous velocity profiles of the incoming upstream flow. Some examples include long-span bridges immersed in an atmospheric boundary layer (BL), underwater pipes near the seabed or subject to strong currents, bridge pillars that are close to the river shore, or buildings in the wake of other upstream buildings in urban areas.

Perhaps the simplest model characterising this situation is the uniform planar shear flow past a circular[1–3] or square[4,5] cylinder, where the streamwise incoming velocity profile is linear. In these conditions, the shear parameter is defined as $K \equiv DG/U_c$, where D is the characteristic length, U_c the upstream streamwise velocity at cylinder mid-height and $G = (\partial u/\partial y)_{y=y_c}$ the dimensional cross-stream gradient of streamwise velocity.

Sometimes the body under scrutiny is placed in the way of a thin shear layer rather than a smooth shear profile. This is the case of objects cast in the near wake of lift-producing devices such as airfoils, stator vanes or rotor blades of compressors, turbines or fans. The rods supporting structural casings of some of these devices are examples of objects subject to this type of incoming flows. It is situations of this kind that we intend to model here by placing a square cylinder in the interface of two streams of different velocities. In fact, the configuration in which a bluff body is placed in the wake of a streamlined body has very seldom been considered in the literature, notable exceptions being the analysis of cylinders in the wake of airfoils[6,7]. Although this problem is different than that of homogeneous upstream shear, the effects of the different velocities seen by the upper and lower sides of the bluff body are still analogous to some extent. The problem at hand falls within the wider class of wake-body interaction[8–12], which deals with objects placed in the usually unsteady though statisticaly symmetric wake of some bluff body. Another fitting problem category, perhaps even more relevant, is the flow past bodies in tandem arrangement[13,14], the one upstream being typically blunt and often also the one downstream, frequently both cylinders. The particular case of an upstream body inducing an asymmetric steady wake on the downstream body as we have here has rarely been addressed despite its intrinsic interest.

The transitions among the various flow regimes past bluff bodies are often characterised through irregularities in the trends that some aerodynamic performance indicators follow upon varying the governing parameters. The recirculation bubble length (l_r) in the square cylinder wake increases fast with $Re \lesssim 50$ while the flow remains steady, reaches a maximum at the onset of vortex-shedding and then quickly recedes (on average) in the interval $Re \in [50, 160]$ until three-dimensionality kicks in[15,16]. The decrease of l_r briefly stagnates for a while across the wake-transition regime for $Re \in [160, 220]$ and

[a)] Electronic mail: fernando.mellibovsky@upc.edu

it is finally resumed at a slowing pace that asymptotically approaches a terminal value for $Re > 1000$[17,18]. Meanwhile, the wake width (W), which is large at the onset of time-dependence, decreases fast while the solution remains 2D, reaches a minimum within the wake transition regime and then gradually recovers to asymptotically stagnate as Re is further increased. The evolution of the drag coefficient (C_d) positively correlates with W, with a minimum precisely located within the wake transition regime[15–17,19–21]. A fair indicator for the expected base pressure coefficient (C_p^b), which decisively influences C_d, is provided by the length of the vortex formation region (l_f)[22,23]. Short formation lengths generate greater suction on the back surface of the object and consequently higher drag is to be expected. Nonetheless, a thorough understanding of C_d trends must necessarily couple the dependence of C_p^b (or l_f) on Re with that of W, which in turn depends on the location where boundary layers separate. Unsteady two-dimensional circular cylinder wakes exhibit a shrinking vortex formation region as Re is increased, but l_f starts growing past the wake transition regime as three-dimensionality develops fully[24]. The increasing trend is however reversed anew as the shear layers become prone to the Kelvin-Helmholtz instability that ends up triggering transition to turbulence[25]. In contrast, l_f (C_p^b) follows a decreasing (increasing) trend over the full Re range for the square cylinder, with an interim vacillation only across the wake transition regime[15,16,18]. C_d decreases with Re for the two-dimensional vortex-shedding solution as W gets smaller, despite the declining trend of l_f. Once the flow has become three-dimensional, the increase in C_d can be ascribed to the fast shortening of the vortex formation region, which now acts concurrently with the slow widening of the wake[18].

The Strouhal number for the time-dependent flow around square and circular cylinders grows steadily as Reynolds number is increased while vortex shedding remains 2D[16]. In the wake transition regime, St experiences a sudden discontinuous drop[15,16] that is later overcome in a second discontinuity[26,27], a feature that passed unnoticed in early square cylinder experiments[19,28]. As for the circular cylinder, the first and second discontinuities are associated to the inception of modes A (with dislocations) and B, respectively[18,26,29]. The analogy in the evolution of St with Re between circular and square cylinders ends at the wake transition regime. While St keeps asymptotically increasing for the circular cylinder until the detached shear layers become unstable to a Kelvin-Helmholtz-type instability at $Re \sim O(10^3)$[25,30], the square cylinder St undergoes a slow decline immediately after the wake transition regime has been overcome and mode-B-type structures pervade the wake[18,20]. The differences are mainly attributable to the effect that the presence of sharp corners has on the location where boundary layers separate to form shear layers. Separation points can freely loiter on the surface of a circular cylinder, both instantaneously or as a consequence of changing parameters such as Re, free-stream turbulence intensity (Tu), aspect ratio ($\Gamma \equiv L_z/D$), blockage ratio ($B \equiv L_y/D$) or end conditions. For a square cylinder, boundary layers are bound to separate at the leading edge corners and are only seen to reattach for very low $Re < 155$, and then only to separate again from the trailing edge corners. Beyond this point, separation seems to invariably occur at the front corners[17] and a saddle point emerges and floats above the rear corners[16,31]. As a matter of fact, the separation bubble debuts at $Re \simeq 100$ (for the average flow fields, slightly earlier if instantaneous fields are considered) at about a third chord distance from the leading edge, such that separation is not initially located at the front corners, but approaches them fast as Re is increased[31]. At very low Re, before the inception of the separation bubble, the flow separates at the trailing edge corners. The relation between the flow topologies past square and circular cylinders has recently been elucidated by the numerical smooth transformation of the former into the latter by gradual rounding of the corners[32].

Upon introducing upstream shear, there is general consensus that the stagnation point on a circular cylinder migrates towards the high-velocity side as the shear parameter K is increased, and this independently of Re[33–42]. The drift induces an acceleration of the flow along the front part on the low-velocity side, which generates a cross-stream pressure force towards it[39]. At the same time, the increase in K delays the separation of the BL on the high-velocity side and advances it on the low-velocity side[33,37]. This has the antagonistic effect of increasing (reducing) the pressure on the low- (high-) velocity side, between the suction peak and the separation point, thus producing a cross-stream pressure force from low- to high-velocity side[39]. At the rearmost portion of the cylinder, the pressure distribution on both sides is approximately flat and dictated by the base point. The net effect, resulting from the addition of the two opposed cross-stream forces at the front and mid chord of the cylinder, is a lift force from high- to low-velocity side that increases linearly with K[40], in accordance with most previous studies[33,36,37,43,44], with some unexplained numerically computed exceptions that produced opposite lift[2,45]. Besides generating the aforementioned lift force, the pressure distribution due to the competing effects of separation and stagnation point locations is such that net torque is generated[46]. The torque acts on the cylinder counter-intuitively with sign opposite to that of the free-stream vorticity, as has been observed in actual experiments[1,3,33].

There is some controversy as to the dependence of C_d of the circular cylinder on the shear parameter. Several experimental[3,37,39,47] and numerical[36,38,48–50] studies have shown a decreasing trend, in some cases marginal, with K. Others[2,43,45] show the exact reverse trend. Free-stream turbulence levels, which are often dependent on the prescribed shear parameter, might be playing an important role in experimental results[39,43].

The drag coefficient has been shown to clearly correlate with the base pressure coefficient at the back of the cylinder also in the presence of upstream shear[36,37,39,40]. The relative contribution of pressure forces to total drag has been found fairly independent of K at any given subcritical Re in the few studies that report it[2,36].

Root mean square of lift fluctuations (C_l') have been reported to slowly increase with K in some cases[36,38,50], decrease in others[33], or even sharply increase to finally decay and disappear altogether at very low Re following the suppression of vortex shedding[2]. Meanwhile, drag fluctuations (C_d') have been shown to either increase[38,50] or to be nearly imperceptible throughout[2]. Base pressure coefficient fluctuations (C_{p_b}') apparently decrease with K[39]. There is also disagreement as to whether St increases with K[45], sometimes after a slight decline at low $K < 0.1$[1,3], clearly decreases[51], marginally decreases[36,38], marginally increases[34], or remains unaffected[39,40].

Upstream shear has been shown in experiments to delay the onset of periodic vortex shedding, the Reynolds number at which the Hopf bifurcation occurs Re^H increasing with K to the point that shedding can be completely suppressed all the way up to $Re < 220$[1]. This effect has also been observed in numerical simulation[2,50]. Other computational studies, however, did not detect the phenomenon despite exploring similar values of the parameters[36,40].

While most two-dimensional studies agree that St decreases for increasing $K \leq 0.2$ for Reynolds numbers $Re \in [Re^H, 250]$[52,53] and even beyond[5,54], experiments and three-dimensional numerical simulation seem to indicate that this trend is overcome for higher values of $Re \in [500 - 1000]$, for which St is unaffected by K[4] or marginally increases[55]. Meanwhile, both $\langle C_l \rangle$ and $\langle C_d \rangle$ decrease at low $Re \lesssim 100$ (the former pointing towards the low-velocity side) and increases instead at high $Re \gtrsim 100$[56], a behaviour that seems to persist at much higher Re for C_l but not for C_d[4], even in two-dimensional simulations for $Re \leq 1500$[5]. There exist however notable two- and three-dimensional numerical studies that have reported positive growing C_l for increasing K at moderate Re[41,56]. The rate of increase of $\langle C_l \rangle$ with K sharpens as Re gets larger, while $\langle C_d \rangle$ becomes quite independent of K for $Re > 200$[4,55]. C_l' and C_d' fluctuations increase both with Re and with K at low $Re \leq 150$[56] and even beyond[41], but are mostly insensitive to K at higher Re[4,5].

A unique secondary three-dimensionalising instability characterised by a single mode[41] is observed in the wake behind a square cylinder subject to upstream shear. This mode arises at $Re \simeq 140 \sim 150$ when $K = 0.2$ and it was initially mistaken for mode B[41] due to its similar wavelength. Its three-dimensional flow structure, however, experiences a half wavelength shift every vortex-shedding cycle, a symmetry which plausibly relates it to a mode C originally found for the uniform flow past a toroidal cylinder[57] and later also past square cylinders at incidence[58], and circular cylinders immersed in homogeneous upstream shear[59]. It seems that the disruption of the top-bottom spatial Z_2 symmetry, favours mode C, which takes precedence over modes A and B.

In the present manuscript, we have chosen to place the square cylinder in a thin shear layer created by a piecewise-constant velocity profile with the discontinuity separating the top and bottom homogeneous streamwise velocities precisely located at cylinder mid-height. The same configuration was previously used by Mushyam and Bergada[60], An et al.[61], although the flow was intentionally kept two-dimensional. This kind of upstream conditions may be obtained experimentally in a wind or water tunnel[62], and the development of the shear layers thus generated have been thoroughly investigated[63–65]. The plate length, the gap between its trailing edge and the cylinder and the bottom stream Reynolds number are kept constant, while the top stream Reynolds number, and with it the top-to-bottom Reynolds number ratio $R \equiv Re_T/Re_B$, has been gradually increased. The linear stability analysis of the asymmetric two-dimensional Kármán vortex flow, the temporal characterisation of the resulting nonlinear solutions and the spanwise-symmetry implications across the wake transition regime were all discussed in detail in a separate study[66]. Here we exploit the same simulation results and place the focus instead on the aerodynamic performances, and their relations with wake topology and statistics.

The paper is structured as follows. The mathematical model is briefly presented in section §II alongside the numerical approach undertaken. Section §III discusses the main aerodynamic performance parameters of the flow. The spatial and temporal characterisation of the flow past the cylinder is then tackled in section §IV, followed by a detailed analysis of the boundary layers on the top and bottom surfaces in section §V. Finally, the main results are summarised and conclusions drawn in section §VI.

II. MATHEMATICAL MODELLING

The geometry consists of a square cylinder of side D placed at zero incidence in the wake of a horizontal splitter plate of negligible thickness that separates two incoming streams with velocities U_T and U_B, above and below, respectively. The flow is governed by the Navier-Stokes equations, which after suitable non-dimensionalisation with length D, the kinematic viscosity of the fluid ν, and the upstream mean/bulk velocity $U = (U_T + U_B)/2$, read

$$\begin{aligned} \frac{\partial \mathbf{u}}{\partial t} + (\mathbf{u}\cdot\nabla)\mathbf{u} &= -\nabla p + \frac{1}{Re}\nabla^2\mathbf{u}, \\ \nabla\cdot\mathbf{u} &= 0, \end{aligned} \tag{1}$$

where $\mathbf{u}(\mathbf{r};t) = (u,v,w)$ is the non-dimensional velocity and $p(\mathbf{r};t)$ the non-dimensional pressure, at a non-dimensional location $\mathbf{r} = (x,y,z)$ and time t. The scalar quantities x (u), y (v) and z (w) are the streamwise,

cross-stream and spanwise coordinates (velocity components).

Figure 1 represents the computational domain with the centre of the square cylinder located at the origin. The domain extends $L_x^u = 9D$, $L_x^d = 25.5D$ and $\pm L_y/2 = \pm 8D$ from the origin in the upstream, downstream and cross-stream directions, respectively. The horizontal splitter plate, of chord-length $L = 6.5D$, starts at the inlet boundary and stretches at mid height leaving a gap of 2D with the front surface of the cylinder. The spanwise extent of the domain has been varied in the range $L_z \in [2.5, 10]$.

A piece-wise constant velocity profile has been prescribed at the Dirichlet inlet boundary with $\mathbf{u} = U_T\,\hat{\imath} = 2UR/(R+1)\,\hat{\imath}$ above the splitter plate and $\mathbf{u} = U_B\,\hat{\imath} = 2U/(R+1)\,\hat{\imath}$ below it, alongside homogeneous Neumann conditions for pressure. The top and bottom boundaries have been treated as slip walls, i.e. $\partial_y u(x, \pm 8, z) = v(x, \pm 8, z) = \partial_y w(x, \pm 8, z) = p_\infty = 0$, while no-slip boundary conditions have been used for the splitter plate and cylinder walls. For the outlet boundary, homogeneous Neumann velocity $(\nabla \mathbf{u} \cdot \hat{\mathbf{n}})(25.5, y, z) = 0$ and homogeneous Dirichlet pressure $p(25.5, y, z) = 0$ have been specified. The incompressible viscous flow has been evolved in time with the Incompressible Navier-Stokes solver implemented in Nektar++, an open source code based on the spectral/hp element method[67]. The velocity correction scheme has been applied for the time evolution, which is made consistent with the second-order temporal accuracy of the numerical scheme by increasing the order of the pressure boundary condition[67,68].

In the streamwise-crossflow plane, a spatial discretisation of 14426 2nd-order quadrilateral elements has been deployed, and a few selected cases run with 3rd order polynomial expansions in order to asses grid independence. Errors in performance monitors are estimated at below 1% (see appendix A). A particularly refined mesh has been setup in the vicinity of the shear layers, boundary layers and the wake to capture the complex dynamics expected there. Along the span of the cylinder, Fourier expansions of 28 to 80 modes have been deployed to fully resolve the three-dimensional features of the flow, by always guaranteeing six orders of magnitude decay in modal energy.

The time step has been set to $\Delta t = 3 \times 10^{-3}$ for two-dimensional cases, and then gradually decreased to 1.2×10^{-3} at the highest-R explored to meet the CFL condition and guarantee sufficient accuracy. Simulations have been ran for over 500 advective time units past all transients before starting collecting data and then evolved for an additional minimum of 40 to 60 vortex shedding cycles (often more) to obtain sufficiently converged statistics.

The method, domain and mesh have been validated against benchmark computations of the homogeneous flow past a square cylinder at comparable values of the Reynolds number, and test runs independently doubling L_x^d and L_y have been performed to quantify the degree to which results are independent of domain dimensions (see appendix A). Aerodynamic performances monitors deviate by less than 0.7% upon doubling L_x, while blockage-induced errors are estimated at less than 2.5% for three-dimensional simulations. Force coefficients r.m.s. values have been found particularly sensitive to blockage effects in two-dimensional computations ($\sim$10% error), but the sequence of bifurcations and the type of solutions found along the way are not qualitatively affected. Convective-type conditions of the Robin type have also been prescribed at the outlet boundary for some test cases but produced no perceptible alteration to any of the aerodynamic performance quantities, thus confirming that the downstream extent of the domain is already sufficiently long to have no impact on the flow field around the cylinder.

The main flow parameters governing the dynamics are the Reynolds number ($Re \equiv UD/\nu$), and the top-to-bottom streamwise velocity ratio ($R \equiv U_T/U_B$). Alternatively, two independent Reynolds numbers, for the top and bottom streams, might as well be defined and used as an alternative set of parameters. In the present study, the bottom Reynolds number is kept constant i.e. $Re_B = 56$ while the top Reynolds number is varied in the range $Re_T \in [56, 301]$. This corresponds to the simultaneous variation of the top-to-bottom velocity ratio $R \in [1, 5.375]$ and bulk Reynolds number $Re \in [56, 178.5]$.

The stability analysis performed by El Mansy et al. [66] revealed that the flow remains two-dimensional for $R \lesssim 3.1$, and that the fastest growing three-dimensional mode in the range $3.2 \lesssim R \lesssim 4.0$ has a characteristic spanwise wavelength $\lambda_z \simeq 2.4$. Further increase in R shifts the preferred wavelength of the instability towards $\lambda_z \simeq 2.1$. Consequently, a spanwise domain of $L_z = 5$ seems a fair choice to capture the dominant mode and allow computation of nonlinear solutions that yield sufficiently accurate first and second order statistics. Nevertheless, a few simulations with $L_z = 10$ have been run to confirm the appropriateness of the spanwise extent.

The lift (F_l) and drag (F_d) aerodynamic forces per unit span are nondimensionalised into force coefficients following $C_l = 2F_l/(\rho U^2 D)$ and $C_d = 2F_d/(\rho U^2 D)$, respectively, while pressure (C_p) and skin friction (C_f) coefficients are derived from the dimensional pressure p and wall shear stress $\tau_w = (\nabla \mathbf{u} \cdot \hat{\mathbf{n}})_w$ according to $C_p = 2(p - p_\infty)/(\rho U^2)$ and $C_f = 2\tau_w/(\rho U^2)$. Superscripts C_x^p and C_x^f on the lift and drag coefficients denote the pressure and friction (viscous) components, respectively.

III. AERODYNAMIC PERFORMANCES

As is the case for any bluff body, the aerodynamic forces acting on the square cylinder are dominated by pressure rather than friction. This is mainly true for drag, as its decomposition into pressure (dotted line)

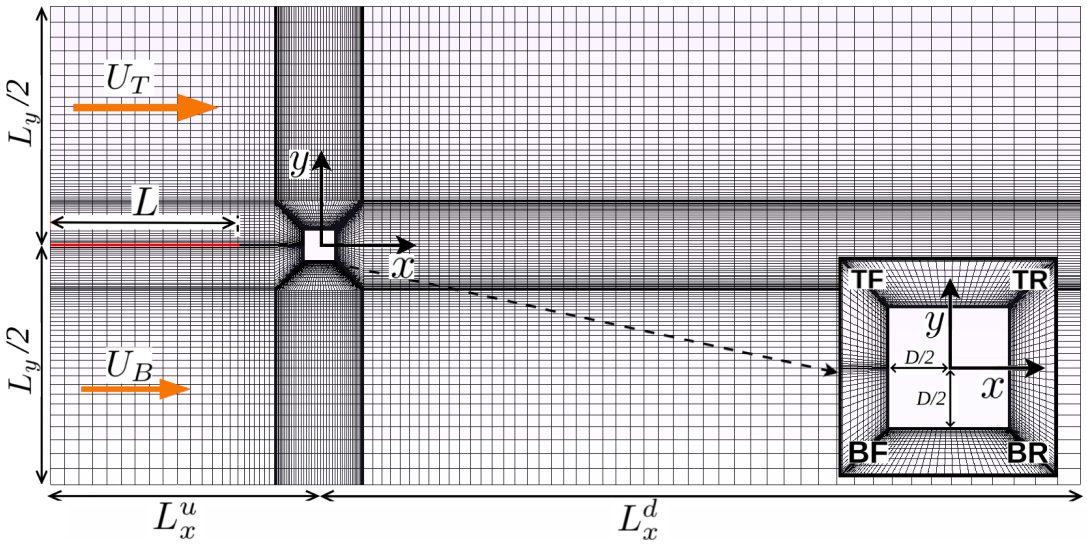

FIG. 1: Sketch of the computational domain and mesh. The square cylinder, of side D, is centred at the origin. The splitter plate (Red), of length L and negligible thickness, starts at the upstream boundary, located at $y = -L_x^u$, and extends horizontally at mid-height. The downstream boundary is located at $y = L_x^d$ and the top and bottom boundaries at $y = \pm L_y/2$. Homogeneous (U_T) and (U_B) velocities are prescribed on the top and bottom portions of the inlet boundary. The domain is periodic along the span for three-dimensional simulations. The mesh is particularly refined in the vicinity of the cylinder where complex phenomena are taking place, and left to relax away from it. The inset shows a detail of the mesh around the cylinder and in the near wake.

and friction (dashed) components clearly shows in figure 2a, but not quite so when assessing lift at low velocity ratios R (figure 2b). The evolution of C_d can therefore be explained mostly in terms of pressure distribution on the cylinder surfaces, while that of C_l requires the combined analysis of pressure and friction. After an initial, barely perceptible decline, C_d starts growing with R, which implicitly involves the increase of both Re and an equivalent shear parameter purposely defined as $K \equiv 2(U_T - U_B)/(U_T + U_B)$. For cylinders subject to homogeneous shear, C_d tends to reduce with K[36,49] and increase with Re[69,70]. Here it seems that the latter effect dominates over the former. The initial decline of C_l with R is sharper than that of C_d, as the friction component C_l^f, which dominates at low R, decreases fast. The net effect is a downforce that is only reversed for higher R, when pressure lift C_l^p starts growing fast and friction lift C_l^p stagnates. This occurs as the flow becomes time-periodic, but the downforce is not overcome, and average positive lift obtained, until after the flow has become three-dimensional for $R > 3.1$. The net downforce has also been reported for square cylinders in homogeneous upstream shear[49,71] for $Re \leq 100$ and $K \leq 0.5$, while for $Re \geq 150$, positive lift has been observed[41,56]. Both observations are perfectly compatible with our results. For completeness, the data of figure 2 is given in table V of appendix B. Once the flow becomes time-dependent, both the lift and drag coefficient start fluctuating. The oscillation amplitudes, denoted with error bars, come mainly from pressure force fluctuation for both C_l and

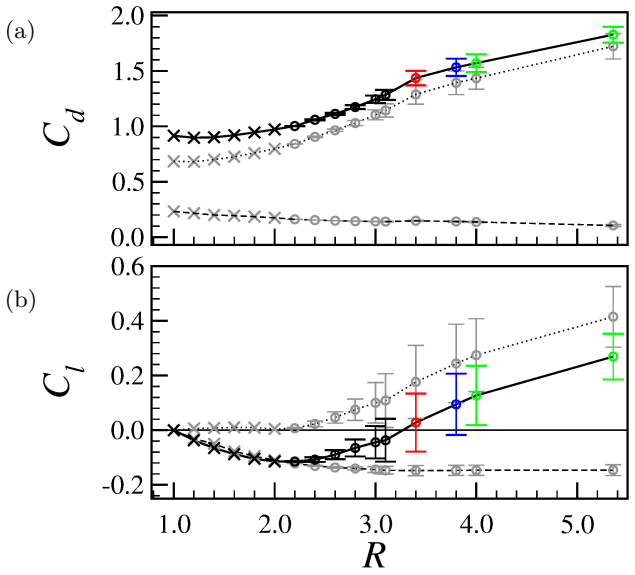

FIG. 2: Averaged Lift and Drag coefficients as a function of the velocity ratio R. (a) Drag coefficient C_d. (b) Lift coefficient C_l. Different symbols denote steady (cross signs) and unsteady (circles) solutions. Colour coding separates 2D (black), 3D periodic (red), 3D period-doubled (blue) and chaotic (green) solutions. Total force coefficient trends (solid lines) are split into their pressure (dotted) and friction (dashed) components.

C_d, with friction force fluctuation barely perceptible.

Figure 3 shows the spanwise- and time-averaged pressure coefficient $\langle C_p \rangle_{z,t}$ distribution on all four cylinder surfaces for a selection of velocity ratios. The graph above the cylinder sketch depicts the $\langle C_p \rangle_{z,t}$ distribution along the top (solid line) and bottom (dashed) surfaces, while that to the right shows the distributions for the front (solid) and rear (dashed) surfaces. The pressure lift (C_l^p) and drag (C_d^p) force coefficients may be readily obtained from assessing the areas enclosed between the lines for bottom and top and for front and rear surfaces, respectively. The $\langle C_p \rangle_{z,t}$ distributions on the top and bottom surfaces are mutually identical for $R = 1$ (yellow), while those for the front and rear surfaces are even-symmetric about the $y = 0$ plane, on account of the reflection symmetry of the problem. As a result, the pressure lift cancels exactly ($C_l^p = 0$), as also does the pitching moment about the centre of the cylinder due to pressure forces ($C_m^p(O) = 0$). The pressure drag coefficient $C_d^p \simeq 0.684$, which is the main contributor to total aerodynamic drag, is already quite important at $R = 1$.

As the symmetry is broken by setting $R > 1$, the $\langle C_p \rangle_{z,t}$ distribution on the top and bottom surfaces become increasingly dissimilar. The evolution for small increasing R is that of generating a positive pressure difference between top and bottom on the back half of the cylinder and a negative one on the front, such that the downforce produced by the front half of the cylinder is just overcome by the net lift generated by the rear half at $R = 2$. At $R = 3$, the whole chord of the cylinder is already producing pressure lift, and the top-to-bottom pressure difference grows fast as R is further increased. The effect on the rear surface of increasing R is, beyond gradually reducing the average $\langle C_p \rangle_{z,t}$, that of slightly dissymmetrising its distribution towards lower (higher) pressures on the TR (BR) corner. The dissymmetry is more prominent on the front side, with a remarkable pressure surge in proximity of the TF corner and a moderate pressure drop at the BF corner. The average $\langle C_p \rangle_{z,t}$ increases sharply on the front surface and, in combination with the slight but steady decrease on the rear surface, accounts for the fast increase of the pressure drag coefficient $\langle C_d^p \rangle_{z,t}$, and, with it, the total $\langle C_d \rangle_{z,t}$. This increasing trend has been observed to persist at much larger Reynolds numbers up to $Re < 1500$[5]. The bulk of $\langle C_l^p \rangle_{z,t}$ is produced on the front half of the cylinder and $\langle C_d^p \rangle_{z,t}$ is strongly biased towards the upper half, an observation already reported in the literature[49,55,56]. Both effects combined result in a strong nose-up (negative) pressure pitching moment $\langle C_m^p \rangle_{z,t} < 0$.

The spanwise- and time-averaged friction coefficient $\langle C_f \rangle_{z,t}$ distributions on all four cylinder walls are shown in figure 4. As was the case for pressure forces, friction forces may also be assessed from areas in these graphs, but now it is the area between each individual curve and the $\langle C_f \rangle_{z,t} = 0$ line that matters. The symmetry of case $R = 1$ has the exact same effects on the $\langle C_f \rangle_{z,t}$ distributions as discussed above for $\langle C_p \rangle_{z,t}$. The friction on the top and bottom surfaces generates a friction drag C_d^f that contributes its share to total drag C_d, while on the front and rear surfaces the upward-pointing friction above the mid plane $y = 0$ compensates exactly the downward-pointing friction below the mid plane, producing no net C_l^f. Friction values are higher on the front surface than on the rear surface. As R is increased in the steady regime, velocities above the cylinder grow and produce higher friction on the top wall, while friction is reduced on the bottom wall. So much so, that at $R = 2$ a separation bubble has appeared on the bottom wall and, with it, a region of forward-pointing friction. The separation point is initially a third chord downstream from the BF corner, but it moves fast towards it as R is increased, an effect that has also been observed for the classic square cylinder configuration as Re is increased beyond the value for which the separation bubble first develops[31]. The friction on the top surface has increased from the symmetric case, but is nonetheless outweighed by the friction drop on the bottom surface. The net effect is a slow decrease in net friction drag C_d^f that is sustained over the full range of R explored. Although the bottom wall friction stagnates at negative values beyond $R = 2$, that on the top wall starts decreasing, and the net effect remains a slow decrease of C_d^f. The magnitude of C_d^f is however much lower than that of C_d^p, which clearly dominates, already at $R = 1$, and the prevalence of the latter intensifies as R is increased. The separation point on the bottom surface moves fast to the BF corner and the reattachment point quickly recedes and disappears, such that the boundary layer is fully detached. This explains why $R = 2$ features about the highest pressures on the bottom surface of all cases considered. The friction forces on the rear surface remain quite low over the full range of R explored, and, though the top-bottom odd-symmetry is broken as the base point moves, some compensation remains between the top and bottom halves. The situation is very different on the front surface. Here the down-pointing friction grows large as the stagnation point moves towards the TF corner, in agreement with all published literature on both square[49,55] and circular[33–36,38,40] cylinders subject to upstream shear. The ensuing net C_l^f is negative and corresponds to a strong downforce. This downforce grows fast at low R, while the net pressure lift C_l^p remains rather low, which results in the initial decline of total lift C_l towards a net downforce. As the velocity ratio is increased beyond $R > 3$, the $\langle C_f \rangle_{z,t}$ distribution on the front face stagnates, while the $\langle C_p \rangle_{z,t}$ distribution difference between bottom and top surfaces grows fast. As a result, C_l^p takes the lead over C_l^f, and the total C_l reverses its trend. Net lift is already being produced by the time $R = 3.4$ is reached.

Performance parameters are strongly linked to a few singular points (lines in 3D) on the object surface, which are in turn related to flow topology. One such class of points is the so-called separation point where the boundary layer developing on a wall detaches from it in the presence of an adverse pressure gradient, thus contribut-

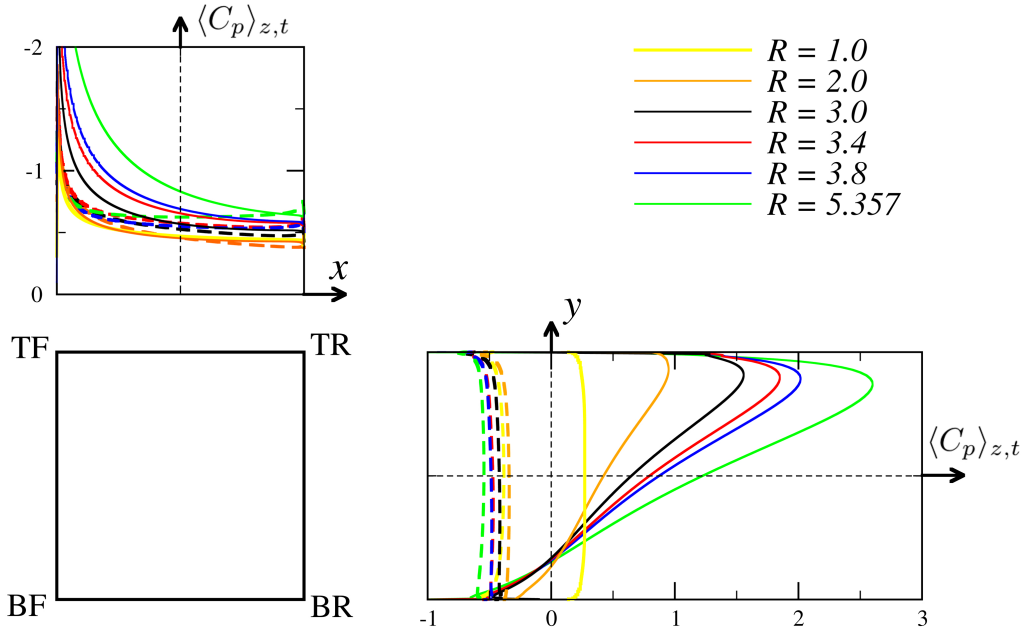

FIG. 3: Spanwise- and time-averaged pressure coefficient $\langle C_p \rangle_{z,t}$ distribution on the front (solid) and rear (dashed) walls (right panel) and on the top (solid) and bottom (dashed) surfaces (top panel).

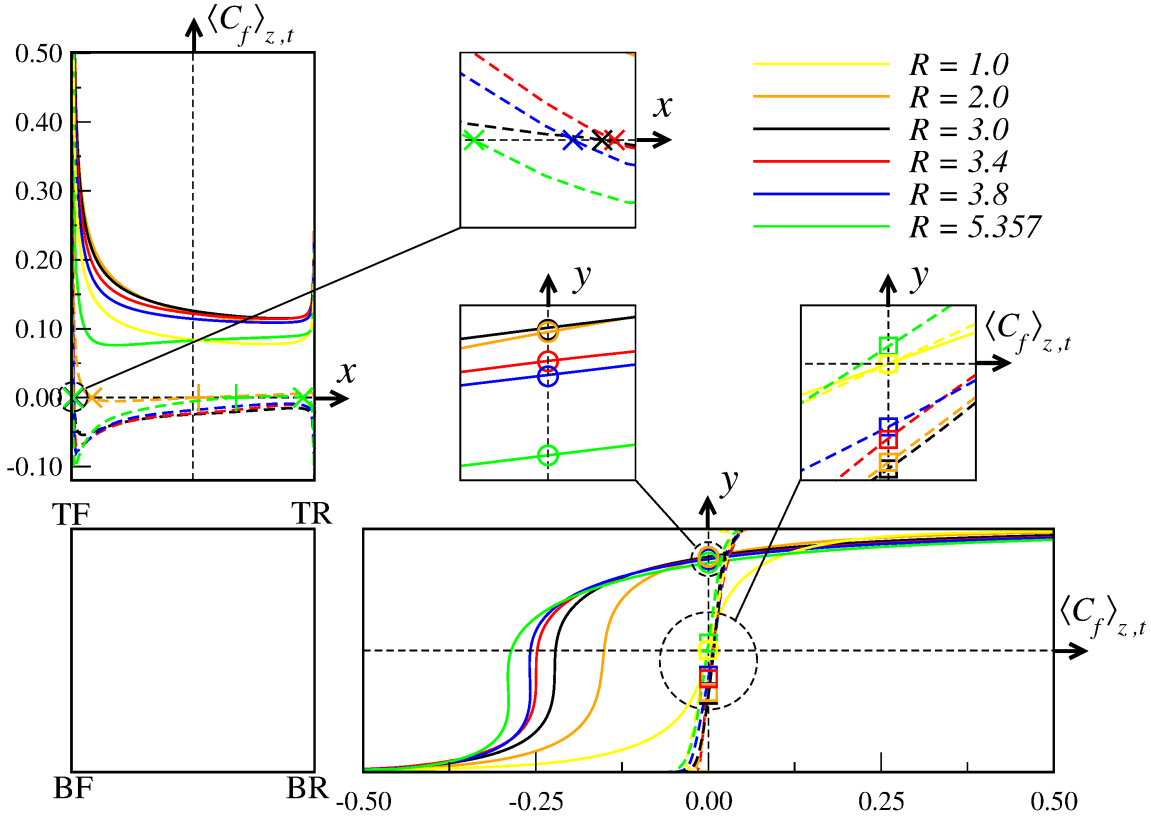

FIG. 4: Spanwise- and time-averaged friction coefficient $\langle C_f \rangle_{z,t}$ distribution on the front (solid) and rear (dashed) walls (both to the right of the square) and on the top (solid) and bottom (dashed) surfaces (top panel). The regions indicated with dashed circles are zoomed in to better identify stagnation, base, separation and reattachment points.

ing to the enlargement of the wake. In the case of the symmetric flow past a square cylinder at sufficiently low Re, the downstream corners, TR and BR, constitute separation points for the boundary layers developing on the top and bottom walls, respectively[19]. The increase of C_p at the BR corner upon increasing R, generates an adverse pressure gradient along the bottom wall that may result in an early separation. Separation points may be detected by the cancellation of wall shear stress and one can be clearly spotted in figure 4 for $R = 2$ (orange cross). In this case, however, the detached boundary layer reattaches shortly after (orange plus sign) leaving behind a small separation bubble. Reattachment points are also identified by a change of sign of friction. Beyond this value of R, reattachment rapidly moves to the BR corner and disappears, while separation migrates to the BF corner and leaves the full bottom wall in detached conditions. At the largest $R = 5.357$, however, the detached flow at BF gets reattached briefly in the rear half of the bottom surface before detaching again slightly upstream from the BR corner.

Two other singular points are the stagnation and base points on the front and rear faces, respectively. A streamline impinges on the former and another one, running upstream, on the latter. A characteristic property shared by both points is that the wall-normal gradient of wall-parallel velocity cancels exactly, and wall shear stress with it. They can therefore be readily identified by looking for zeroes along the C_f distributions on the front and rear surfaces. The spanwise- and time-averaged stagnation point location for the several R inspected in figure 4 have been duly marked in the graph to the right of the cylinder sketch (circles). The impinging streamline hits the front face at $y_s = 0$ for the symmetric case $R = 1$ but rapidly climbs to about $y_s \simeq 0.4$ for $R = 3$, close to the TF corner, and remains pretty much unaltered thereafter. Meanwhile, the base point (squares) also starts exactly at the mid plane $y_b = 0$ on the rear face for $R = 1$, but moves steadily down as the velocity ratio is increased to moderate values. The highest case $R = 5.375$, however, has the base point relocated back close to the mid plane.

So far we have discussed separation, reattachment, stagnation and base points from the point of view of average flow fields, but they will of course evolve dynamically for time-dependent solutions. Separation bubbles, when present, fluctuate in size and may occasionally form and disappear as a matter of course. Three-dimensionality renders the situation even more complex, and friction cancellation may occur without separation. Here three-dimensionality is only mild, as the base flow is two-dimensional and spanwise-dependence is only triggered by instability of an already time-dependent solution. The effect is that of introducing an undulation along the span of separation, reattachment, stagnation and base lines rather than modifying their topology altogether.

Figure 5 illustrates the time dependence of the stagnation and base point locations on the square cylinder front and rear walls for a two-dimensional periodic solution at $R = 3$. The C_f distribution on the front wall appears rather steady, as clear from the sharp solid line that represents it. No time fluctuation (gray shading) is apparent to the naked eye. The stagnation point (circle) is biased toward the TF corner and fluctuates imperceptibly. Some time dependence is instead already discernible on the top and bottom wall distributions of C_f, but it is on the rear wall that unsteadiness presents itself at its wildest. The base point (square) is, on average, slightly below the mid plane, but its location fluctuates from very close to the BR corner to slightly above the mid plane.

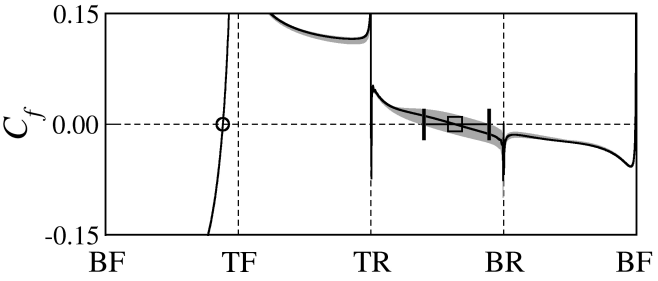

FIG. 5: Friction coefficient C_f distribution on the square cylinder walls for a two-dimensional periodic solution at $R = 3$. Shown are the time average (solid black line) and the time-fluctuation amplitude (gray shading). Symbols indicate the average location of the stagnation (circle) and base (square) points, while error bars delimit fluctuation.

The time- and spanwise-averaged location of stagnation (plus signs and circles) and base (crosses and squares) points has been plotted in figure 6a. The thick error bars denote time-fluctuation amplitude of the spanwise-averaged instantaneous location. Spanwise modulation is further indicated by the lighter-colour thin error bars for instantaneous three-dimensional solutions with maximum, minimum and mean spanwise-average. The stagnation line is fairly straight and steady, while the base pressure line oscillates with rapidly increasing amplitude once time-dependence sets in. Its spanwise modulation, however, is only mild for the three-dimensional periodic and early chaotic solutions, but becomes clearly commensurate with time-amplitude as chaos develops for high values of R. Both the stagnation and the base points start at the mid plane for $R = 1$ on account of the problem symmetry. The stagnation point climbs fast towards the TF corner as R is increased, saturates at about $y_s \simeq 0.39$ across the onset of time-dependence, and then very slowly recedes with the advent and development of three-dimensionality. Fluctuations, when present, are always nearly imperceptible. Meanwhile, the base point steadily drifts towards the BR corner and reaches a minimum, on average, at about $R \simeq 2.8$, from which point gradually recovers and has already crossed to above the mid plane for $R \gtrsim 5.3$. With the onset of time dependence, the spanwise-averaged time-fluctuation amplitude

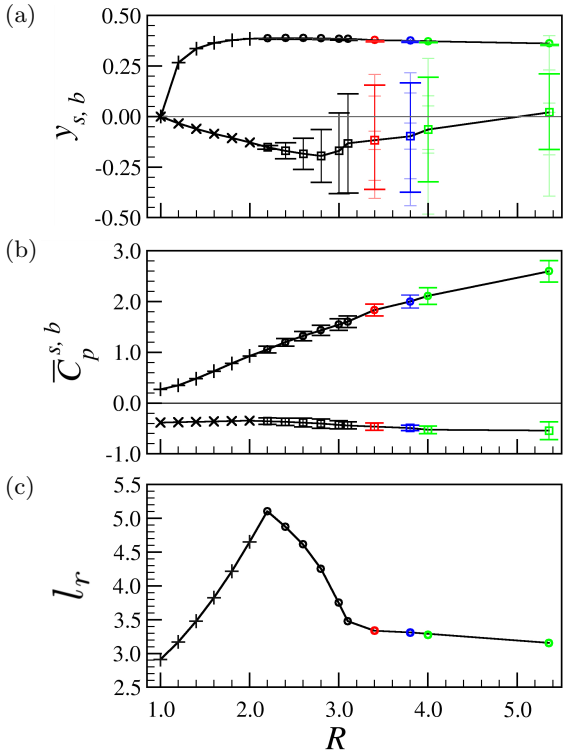

FIG. 6: (a) Stagnation (y_s, plus signs and circles) and base (y_b, crosses and squares) point location as a function of R. (b) Corresponding pressure coefficient values (C_p^s, C_p^b). (c) Recirculation bubble length l_r. Colours as for figure 2 (Base point data replaces crosses and squares with plus signs and circles, respectively). The thick error bars denote time amplitude of the spanwise-average value, while the thin error bars in panel (a) convey spanwise modulation at three particular instants corresponding to maximum, minimum and an mean value of the spanwise average.

grows fast, reaches a maximum once three-dimensionality kicks in and then starts declining, albeit only slowly. At its most unsteady, the spanwise-averaged base point meandering covers over half the rear wall surface along a full solution period. Taking spanwise dependence into consideration it becomes however apparent that the base line locally reaches far beyond the spanwise-averaged location amplitude, and fairly close to the TR and BR corners at certain spanwise locations and time instants along its evolution. While the spanwise-averaged base point location reverses its increasing amplitude trend beyond the onset of chaotic dynamics, the base line sweeps over an ever increasing extension of the rear cylinder surface. The pressure coefficients at the spanwise-averaged stagnation C_p^s and base C_p^b points, shown in figure 6b provide a fair indicator of pressure -and total- drag trends. C_p^s starts at a fairly low value for $R = 1$ and escalates monotonically to increasingly large values as R is raised. C_p^b debuts with a similar but negative magnitude that increases rather slowly while the solution is steady. The onset of time dependence brings a slow decline with it that settles at a nearly constant value for large R. Despite the wild meandering of the base line, the base pressure fluctuation amplitude remains moderate. The raw data used in producing figure 6 has also been reported in table V of appendix B.

IV. WAKE TOPOLOGY AND DYNAMICS

The spanwise- and time-averaged flow fields for a few selected values of R are shown in figure 7. Both the pressure coefficient (C_p, left) and the spanwise vorticity (ω_z, right, along with streamlines) are steady, spanwise-independent and retain the symmetry of the problem for $R = 1$. While the former is even-symmetric about the mid plane, the latter is odd-symmetric. The highest C_p is recorded at the TF and BF corners and maximum $|\omega_z|$ occurs in their close neighbourhood. Away from these corners, C_p is positive ahead from the front wall and negative on all other three walls and into the wake. Streamlines, which are also symmetric, unveil the existence of a large recirculation bubble in the near wake of the cylinder. The streamlines issued from the TR and BR corners meet at a point along the wake centreline whence the streamline that impinges on the base point at the back of the cylinder is issued, along with another streamline leaving downstream to infinity. Velocity necessarily vanishes at the intersection of streamlines, such that the flow at this point is quiescent. The three streamlines connecting this quiescent flow point with points TR, BR and base at the back of the cylinder, together with the rear wall, delimit two mutually symmetric enclosed regions or lobes that do not exchange mass with each other or with the outer flow field. Within these two lobes, fluid particles are trapped and recirculate. The symmetric two-lobed recirculation region is typical of the wake past circular and square cylinders in homogeneous flow at all Re, provided that sufficiently long runs are averaged in the case of time-dependent and chaotic solutions.

A very mild increase to $R = 1.2$ already dissymmetrises the flow field, particularly so the streamlines arrangement. The lower enclosure, which is bound by the streamline now uneventfully connecting the BR corner with the base point, remains attached to the rear wall and shrinks. The upper enclosure detaches instead but remains an enclosed region containing the quiescent flow point at the most downstream location on its boundary. The streamline issued from the TR corner extends now indefinitely downstream, as does the one issued from the quiescent flow point. The streamline that arrives to this point from below does no longer come from the BR corner but from the upstream flow, barely avoiding the cylinder bottom wall. The upstream fluid particles enclosed between this streamline and the one impinging on the stagnation point fly below the cylinder, surround the lower lobe in an anti-clockwise fashion, approach the rear wall above the base point, and then turn clockwise

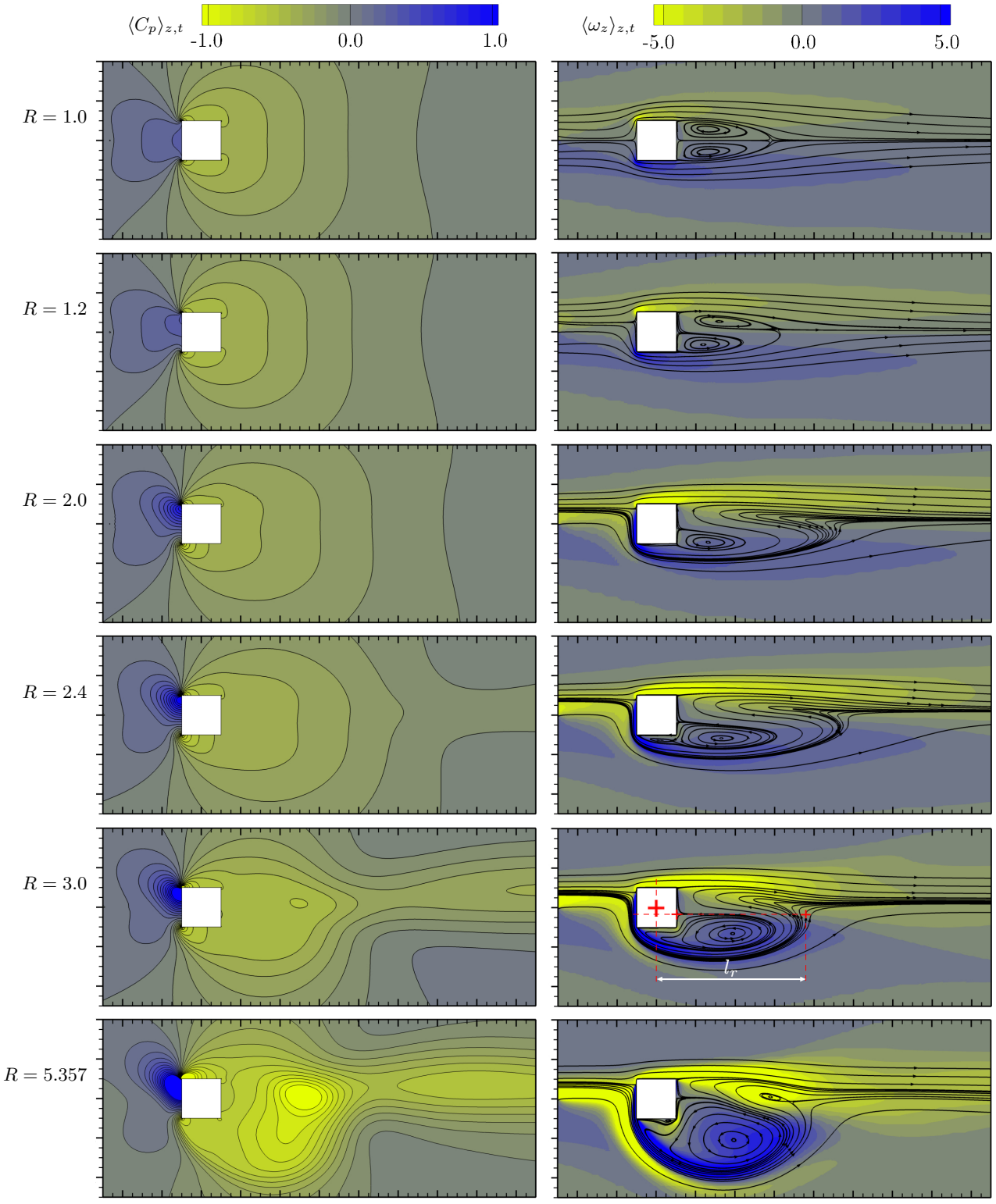

FIG. 7: Spanwise- and time-averaged flow fields. Shown are the pressure coefficient $\langle C_p \rangle_{z,t}$ (left) and spanwise vorticity $\langle \omega_z \rangle_{z,t}$ (right, along with a few streamlines) fields for increasing velocity ratio R (top-to-bottom).

to overfly the upper lobe before being released into the far wake free to travel downstream.

The detached upper lobe shrinks fast and has utterly disappeared by the time $R = 2$ is reached. The implosion of the recirculation enclosure occurs for $R \in (1.4, 1.6)$ and thereafter only the fluid particles within the attached lower lobe remain trapped in the near-wake flow field. The pressure on the rear surface remains negative but the suction is milder. The stagnation point has clearly climbed on the front wall and a pressure surge becomes plainly visible. The negative spanwise vorticity of the upper wall BL has intensified and extends along the shear layer detached from the TR corner. Positive vorticity informs of a strong BL developing from the stagnation point downwards along the front surface and of its detachment, if only partially, on the bottom wall. Here, a small separation bubble is barely perceptible.

The lower lobe grows, now on average, given the time-dependent nature of the solutions, as the velocity ratio is increased beyond $R > 2$. The streamline impinging at the base, which has moved below the mid plane, is no longer issued from the BR corner but from a point that has drifted upstream on the bottom wall until reaching the BF corner. Meanwhile, the rightmost point where the streamlines reaching the wake from the upstream region bend upward and circulate upstream approaches the rear wall of the cylinder. At $R = 5.357$, well into the time-dependent three-dimensional regime, the only remaining time- and spanwise-averaged enclosed recirculation region has grown large in the cross-stream direction and a strong shear layer has developed on its lower boundary. Partial reattachment occurs on the bottom wall.

Bluff bodies present a well defined (statistically averaged) recirculation bubble provided a specular symmetry about the mid plane exists. Defining a recirculation bubble length (l_r) for the upstream-sheared-flow past a square cylinder is therefore not straightforward, because most reversed flow occurs indeed outside of any recirculation bubble. We have chosen to do so by measuring the horizontal distance from the cylinder to the rightmost point in the average flow field where streamwise velocity vanishes, *i.e.* the rightmost inflection point on a streamline presenting purely cross-stream velocity. Thus measured, l_r is seen to increase fast while the solution remains steady two-dimensional (see figure 6c) and then $\langle l_r \rangle_t$ decreases sharply, on average, as time dependence sets in. This sharp crest of l_r at the onset of time-dependence has also been observed upon increasing Re for the homogeneous flow past a square cylinder[17] and has been ascribed to the enhancement of momentum transport into the wake by the unsteady flapping of the shear layers issued from either side of the cylinder[72]. The fast decline is dampened by the inception of three-dimensionality, and $\langle l_r \rangle_{z,t}$ recedes very slowly as R is further increased.

Figure 8 shows instantaneous flow fields at 8 equispaced time-instants along a full vortex-shedding cycle for $R = 2.2$, 2.4 and 3.0, the time origin having been set at the crossing of the Poincaré section defined by $C_l = \langle C_l \rangle_t$, $\dot{C}_l > 0$. For $R = 2.2$, just after the onset of time periodicity, the dynamics seem to consist of a mere fluctuation about the mean flow fields depicted in figure 7. The upper lobe of recirculated flow, which has disappeared on average, exists however instantaneously as the closed streamlines indicate. It is periodically created just downstream from the upper half of the rear wall ($t = 0$), grows there for about half a period (until about $t = T/2$), and then shrinks and disappears when advected downstream by the forming Kármán vortex ($t = 7T/8$). In the mean time, the lower lobe remains attached to the rear wall of the cylinder with its size pulsating periodically. If anything, it may seem to periodically merge with and split from the small recirculation bubble left on the bottom wall by the early detachment of the boundary layer developing on it. The clockwise vortices shed downstream along the wake form in the oscillating motion of the top shear layer. As vorticity concentrates in the vortex-formation region towards the downstream end of the shear layer, the immediately upstream region is depleted, the shear layer conspicuously thinned, and the formed vortex finally left free to tear apart. Unlike what happens in the classic space-time symmetric vortex-shedding regime, no synchronous anti-clockwise vortices are formed here in the bottom shear layer that can pair up with those shed form the top. While clockwise vorticity concentrates in strong monopolar vortices, anti-clockwise vorticity remains stretched along an elongated thin layer that surfs below the top vortex street for some distance (the lower the R, the longer the distance) before either dissipating or being swallowed into one of the clockwise vortex cores. This street of merely negative vortices issued from the TR corner, which become rounded in shape as R increases, has been consistently observed to occur behind both circular[38,40,51] and square[41,49,54,55] cylinders immersed in upstream shear.

At the slightly higher $R = 2.4$, vortex shedding proceeds much in the same way as for $R = 2.2$, but the instantaneous recirculation lobes exchange their roles for a brief period between $t = T/8$ and $3T/8$, during which the upper lobe is the one attached to the rear wall of the cylinder and the lower lobe separates. Separation is always followed by downstream advection, ensuing shrinkage and eventual disappearance. The snapshot at $t = T/8$ is very closely taken at one of these periodic events of role-exchange, while the other takes place some time in between $t = 3T/8$ and $T/2$. The former is very clear as to the underlying mechanism: a quiescent flow point forms instantly to redistribute the streamlines bounding the upper and lower lobes. The streamline impinging on the base point is thereby disconnected from the streamline issued from the TR corner and spliced to that impinging on the separation point on the bottom wall (the lower lobe comprises also the separated region on the bottom wall in this regime).

At $R = 3$, the dynamics does not change qualitatively, but the vortices are stronger and shed earlier and closer to the rear wall of the cylinder. Although the upper

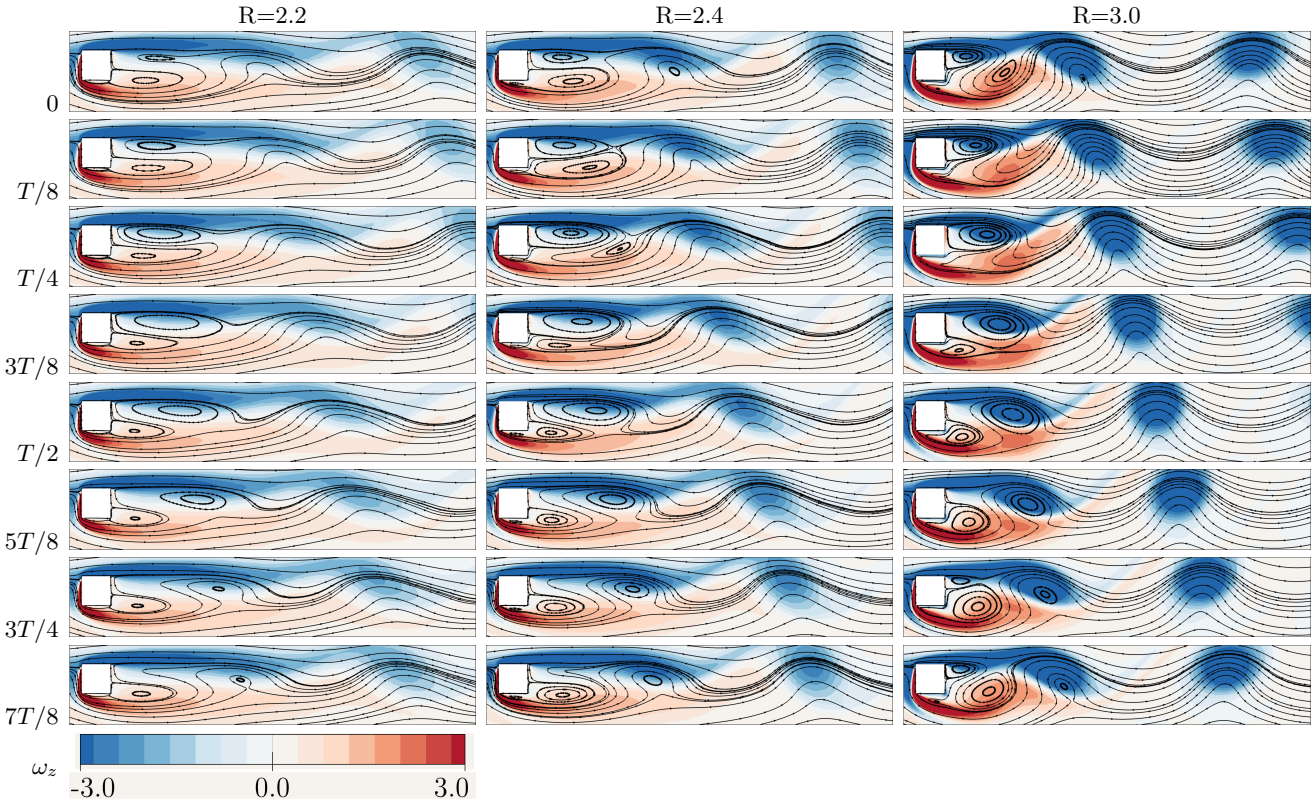

FIG. 8: Wake vortex dynamics. Instantaneous streamlines and spanwise vorticity contours ($\omega_z \in [-3, 3]$, blue to red) over a complete vortex-shedding cycle for velocity ratios $R = 2.2$, $R = 2.4$ and $R = 3.0$. The time origin is set by the crossing of the Poincaré section defined by $C_l = \langle C_l \rangle_t$, $\dot{C}_l > 0$.

lobe remains attached for about half a cycle, its active dynamics, which consist of rapid nucleation, explosive growth and violent pull by the vortex shedding mechanism, leaves no trace of it upon time-averaging of velocity fields. Spanwise-averaging of three-dimensional cases beyond $R > 3$ does not add new time-dynamics features that are worthy of notice. The period-doubling that results from the spanwise-invariance disruption at $R = 3.4$ is suppressed by averaging, the instantaneous spanwise-averaged fields repeating every vortex-shedding cycle exactly as for $R = 3$. Meanwhile, the second (legitimate) period doubling at $R = 3.8$, although introducing a dynamically relevant subharmonic frequency to the flow, is barely identifiable to the naked eye by mere inspection of pressure, velocity or vorticity spanwise-averaged fields. For a detailed account of the bifurcation sequence leading to chaotic dynamics, including all symmetry considerations, see El Mansy et al. [66].

Reynolds stresses provide the means to further characterise the velocity fluctuations of time-dependent solutions and better understand vortex formation and mixing processes in the wake. Figure 9 depicts correlations of in-plane velocity fluctuations, suitably averaged in the spanwise direction for three-dimensional solutions. The streamwise velocity fluctuations self-correlation $\langle u'u' \rangle$ is employed in the definition of vortex formation length. Pressure drag C_d^p -and therefore also drag C_d- of bluff bodies is tightly coupled to the pressure coefficient $\langle C_p \rangle_{z,t}$ at the base point, which is in turn intimately related to the vortex formation length l_f. Long vortex formation regions are associated with a base pressure increase on the rear wall of the bluff body and thus contribute to drag reduction[22,23]. In top-down symmetric problems, the symmetry is statistically preserved in a time-averaged sense and a unique vortex formation length might be defined in the wake[25,73,74]. The symmetry disruption introduced by $R \neq 1$ dissymmetrises the spanwise- and time-averaged fields both of mean and second moments. Accordingly, the top (l_f^T) and bottom (l_f^B) vortex formation lengths are independently defined as the horizontal distances from the centre of the object (the square cylinder in our case) and the streamwise location with maximum $\langle u'u' \rangle$ above and below the horizontal mid plane, respectively. Additionally, vertical distances for top (h_f^T) and bottom (h_f^B) peaks might be defined in order to gauge the interaction between top and bottom forming vortices in the near wake.

Thus defined, vortex formation length is always slightly shorter on the top shear layer as compared to bottom ($l_f^T < l_f^B$), which, in addition with the higher $\langle u'u' \rangle$ peak level, is an indication that the top shear layer has a larger share in driving the wake instability. As R

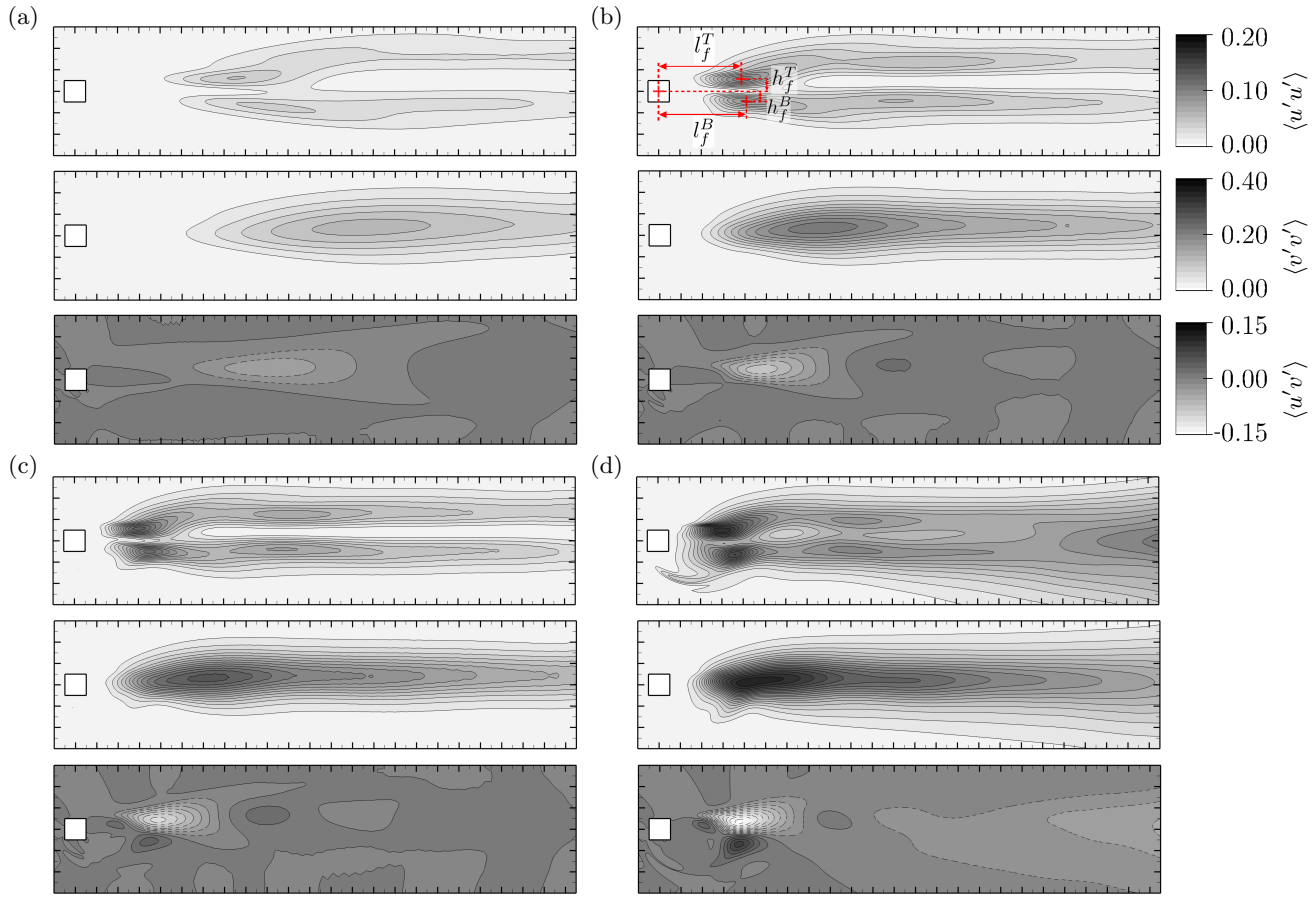

FIG. 9: Near-wake Reynolds stresses $\langle u'u' \rangle \in [0.0, 0.2]$ (top) in steps $\Delta\langle u'u' \rangle = 0.01$, $\langle v'v' \rangle \in [0.0, 0.4]$ (middle) in steps $\Delta\langle v'v' \rangle = 0.02$ and $\langle u'v' \rangle \in [-0.15, 0.15]$ (bottom) in steps $\Delta\langle u'v' \rangle = 0.015$ for (a) $R = 2.4$, (b) $R = 3.0$, (c) $R = 3.4$ and (d) $R = 5.357$.

is increased, the peak $\langle u'u' \rangle$ Reynolds stresses intensify and move gradually upstream on both shear layers. The wake centre line remains fairly insensitive to streamwise velocity fluctuations until sufficiently large values of R, but the advent of chaotic dynamics boosts mixing across the wake width and rather large $\langle u'u' \rangle$ occurs around the horizontal mid plane. The double peak in the cross-stream profiles in the near wake develops into a single, fairly symmetric peak in the mid to far wake.

Cross-stream velocity fluctuations self-correlation $\langle v'v' \rangle$ peak some distance downstream from the vortex formation region. It is here that vortices acquire their maximum strength driving fluid upwards and then downwards upon passing. This enhances the mixing that results in the symmetrisation of the $\langle u'u' \rangle$ cross-stream profiles somewhat downstream on the wake and at sufficiently high values of R. Streamwise-cross-stream velocity cross-correlations $\langle u'v' \rangle$ remain low and mainly negative for moderate values of R, with a peak halfway between the upper maximum for $\langle u'u' \rangle$ and that for $\langle v'v' \rangle$. The sign responds to the fact that a negative cross-stream velocity fluctuation brings high velocity fluid from above the wake into the wake, which accounts for a positive streamwise velocity fluctuation. The product of the two fluctuations produces $\langle u'v' \rangle < 0$. In the chaotic regime, a second peak, this time positive, appears below the negative one. In this case, it is a positive cross-stream velocity fluctuation that brings low velocity fluid from below the wake into a region where the streamwise velocity is on average negative. The ensuing streamwise velocity fluctuation is therefore also positive and so is $\langle u'v' \rangle > 0$.

Figure 10 shows the dependence of the vortex formation region size on the velocity ratio R. It becomes clear how the vortex formation region is very large and very asymmetric for top and bottom shear layers upon the onset of time-dependence but quickly shrinks as R is increased. The contraction soon saturates and the formation region length remains fairly constant at $l_f^T \lesssim l_f^B \simeq 4$. This behaviour is analogous to that observed for a square cylinder with symmetric inflow conditions upon increasing the Reynolds number[18]. In any case the inverse correlation of the vortex formation length $l_f^{T,B}$ with the base suction coefficient $-\langle C_p^b \rangle_{z,t}$ (see figure 6b) is obvious, so that upstream shear does not seem to interfere with the physical mechanism that links both variables in the wake of other bluff bodies.

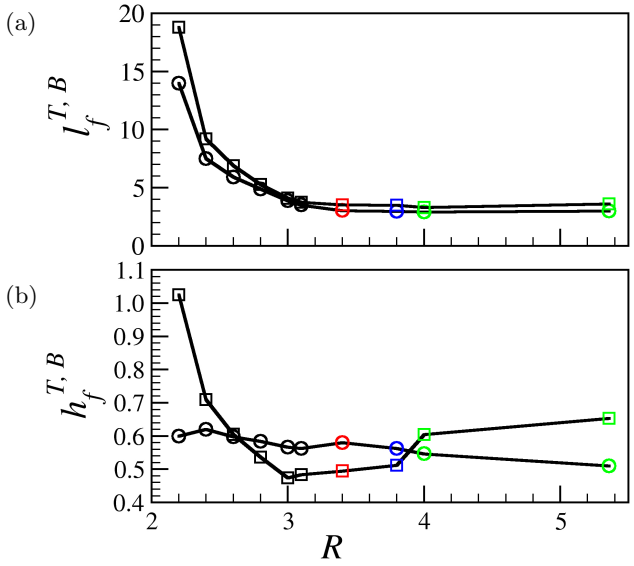

FIG. 10: (a) Top (l_f^T, circles) and bottom (l_f^B, squares) vortex formation lengths as a function of velocity ratio R. (b) Cross-stream distances to mid plane of top (h_f^T) and bottom (h_f^B) Reynolds stress $\langle u'u' \rangle$ peaks. Colour coding as for figure 2.

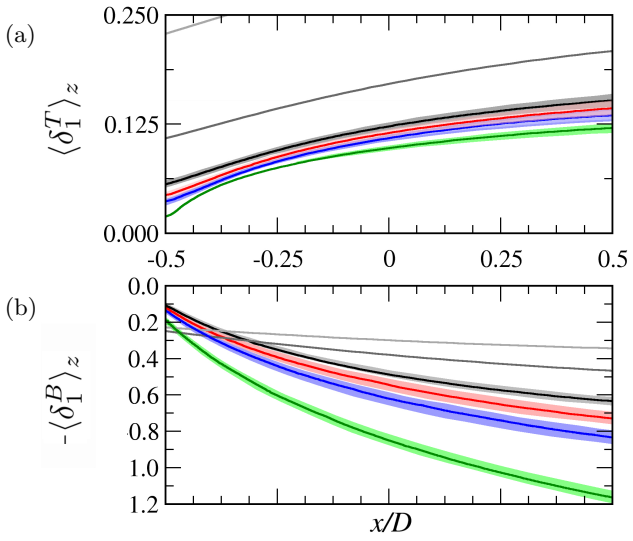

FIG. 11: Time- and streamwise-averaged (for three-dimensional solutions) displacement thickness $\langle \delta_1^{T,B} \rangle_z$ along (a) top and (b) bottom walls for velocity ratios $R = 1$ (light gray), 2 (dark gray), 3 (black), 3.4 (red), 3.8 (blue) and 5.357 (green). Lines indicate average, while shaded regions denote time-fluctuations.

The top vortex formation vertical location with respect to the mid plane h_f^T remains rather aligned with the top surface for all R, perhaps with a slight trend of approaching alignment from above. Meanwhile, the bottom vortex formation location h_f^B debuts far away from the mid plane at the onset of time dependence and then approaches it as R is increased. For a short range around $R \simeq 3$, the vortex formation region gets in the shadow of the cylinder with $h_f^B < 0.5$, but the advent of chaotic dynamics pushes it back into exposure at $h_f^B \simeq 0.6$.

Table VI in appendix B lists the peak values and corresponding location of the Reynolds stress fields $\langle u'u' \rangle$, $\langle v'v' \rangle$, $\langle u'v' \rangle$ and $\langle w'w' \rangle$ of figure 9.

V. BOUNDARY LAYERS ON THE CYLINDER SURFACES

The instantaneous displacement thickness, which quantifies viscous blockage in terms of massflow reduction of the boundary layers developing on the top and bottom surfaces are computed as

$$\delta_1^{T,B}(x,z;t) = \int_{y_{T,B}=\pm 0.5}^{\pm 0.5(1+2\delta^{T,B})} 1 - \frac{u(x,y,z;t)}{u_e^{T,B}(x,z;t)}\, dy \quad (2)$$

and shown in figure 11 for a range of velocity ratios. The maximum streamwise velocity $u_e^{T,B}(x,z;t) = \max_y u(x,y^{\pm},z;t)$ is used as the inviscid outer flow velocity at location (x,z), and the boundary layer thickness $\delta^{T,B}$ is interpreted as the cross-stream distance from the wall to the point where this maximum velocity is reached. For $R = 1$ (light gray), the boundary layers on the top and bottom surfaces are symmetric and rather thick. Thickness is not negligible at the leading edge. The boundary layers developing on the front wall at either side of the stagnation point make their presence conspicuous as they turn around the TF and BF corners and initiate the top and bottom boundary layers with finite thickness. An increase of the velocity ratio to $R = 2$ (dark gray), thins the top boundary layer on account of the higher local Reynolds number Re_T and thickens the bottom one. This trend persists for increasing velocity ratios and is particularly remarkable on the bottom boundary layer as separation boosts the viscous blockage effect and near-wall massflow is not only reduced but reversed. At $R = 3$ (black), time dependence ensuing from the wake instability starts making its effects visible on both top and bottom boundary layers. Time fluctuations are discernible (shaded region) but not prominent. Oscillation amplitude grows with R but remains rather small up to fairly large values, which suggests that the boundary layers are quite stable and their flapping is driven by a foreign instability mechanism inherent to the wake, further downstream. The bottom boundary layer is the thickest and features the largest oscillation amplitude of the two across the full exploration. As a matter of fact, the boundary layers thickness positively correlates with the base point position and intensity at the back of the cylinder, the stagnation point comfortably established in the vicinity of the TF corner for velocity ratios as low as $R > 1.5$. The pressurisation of the BR corner as the base point moves down for increasing R thus induces an

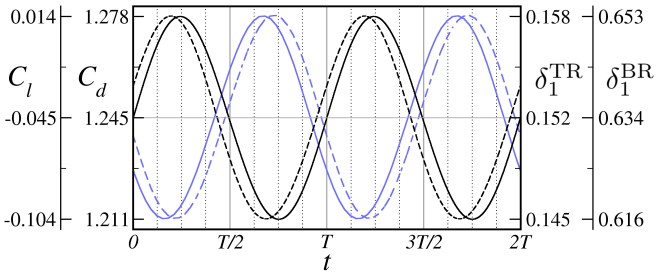

FIG. 12: Dynamic evolution of the lift C_l (Black solid) and drag C_d (Black dashed) coefficients, alongside that of the displacement thickness at the trailing corners for both the top $\delta_1^{\rm TR}$ (Blue solid) and bottom $\delta_1^{\rm BR}$ (Blue dashed) boundary layers developing on the top and bottom square cylinder walls. Times series correspond to the two-dimensional solution at $R = 3$, with corresponding $T = 6.47$.

adverse pressure gradient along the bottom wall that accounts for the thickening of the boundary layer and its eventual separation. Conversely, the pressure reduces on the TR corner, thus contributing to a more favourable pressure gradient and the thinning of the boundary layer on the top wall. Furthermore, both boundary layers flap synchronously with the meandering of the base point once the flow has become time-dependent.

The time evolution of the top ($\delta_1^{\rm TR}(z,t) = \delta_1^T(0.5,z;t)$, solid blue line) and bottom ($\delta_1^{\rm BR}(z;t) = \delta_1^B(0.5,z;t)$, dashed blue) boundary layer displacement thicknesses at the respective trailing edge corners are presented in figure 12 for the two-dimensional solution with $R = 3$. The dynamic lift (C_l, solid black) and drag (C_d, dashed black) coefficients are also shown along the same two complete vortex-shedding cycles for reference. The bottom boundary layer thickness has a delay of about $\Delta\phi \simeq 20^\circ$ with respect to the top, their evolution being close to but not quite synchronous. This is very different from the usual space-time symmetric Kármán vortex street, for which the respective displacement thicknesses are in exact phase opposition, with $\Delta\phi = \pi$, as the shear layers flap synchronously. The force coefficient signals are practically in opposition of phase with the boundary layer displacement thicknesses. C_d is nearly maximum for minimum $\delta_1^{\rm TR}$, and C_l peaks when $\delta_1^{\rm BR}$ is at its valley. The C_l signal follows behind C_d with a phase lag $\Delta\phi \simeq 22^\circ$. Counter-intuitively, C_d is lowest when $\delta_1^{\rm TR}$ and $\delta_1^{\rm BR}$ are both close to their respective peaks, which would seem to misleadingly indicate that the wake width should be largest. In reality, a large boundary layer thickness, particularly that on the top surface, is an indication of a milder favourable pressure gradient, meaning that the base pressure is comparatively large and, therefore, wake drag accordingly low. Regarding C_l, it must be borne in mind that time oscillations are pressure dominated, while cross-stream shear forces remain very stable in time (see figure 2). Fluctuations are therefore almost exclusively the result of top-bottom surface pressure differences. The mean $\langle C_l \rangle$ is in fact a net downforce because down-pointing friction dominates, particularly so on the front surface, but the maximum instantaneous value periodically crosses into slightly positive C_l. It would therefore seem that the drop in base pressure that boosts drag and thins the top and bottom boundary layers has a larger impact on increasing suction on the top surface than on the bottom, thus generating a larger positive pressure difference. The reason for this is that the vortices shed from the top are way stronger than those forming at the bottom, which, as already pointed out upon inspection of figure 8, dissipate fast once freed into the wake. As it happens, C_d grows while the strong vortex forming from the top shear layer remains attached to the rear wall, and peaks at about $T/4$ as it becomes strongest. The resulting lowest base pressure that generates maximum C_d is therefore confined to the top half of the rear wall (actually the portion bounded between the TR corner and the base point) and therefore induces a larger pressure reduction on the top surface than it does on the bottom. Consequently, a net positive pressure lift occurs that brings C_l to its maximum. Minimum C_l correspondingly occurs at around $3T/4$, when the bottom vortex is strongest while still attached, but the associated pressure is comparatively high with respect to the lowest pressure induced by the top vortex, the bottom vortex being weaker, and the C_d happens to be close to its minimum. For space-time symmetric Kármán vortex shedding, the top and bottom vortices induce the exact same peak suction pressure on the top and bottom rear halves of the rear wall, respectively, as they reach their strongest attached stages, such that minimum and maximum C_l are related by a mere change of sign and the same exact value of C_d results in both cases. Consequently, while C_l oscillates with the same frequency of the actual solution, C_d has double the frequency. At $R = 3$ the asymmetry is large enough that there is no trace left of the original double frequency on the C_d signal.

In order to correlate the space-time evolution of the boundary layers with wake structures and force coefficients, the instantaneous displacement thickness of Eq. (2) is computed at the TR and BR corners and additively decomposed into their spanwise average $\langle\delta_1\rangle_z$ and spanwise modulation $\hat{\delta}_1$ components as

$$\begin{aligned}\delta_1^{\rm TR,BR}(z;t) &= \delta_1^{T,B}(0.5,z;t) = \\ &= \langle\delta_1^{\rm TR,BR}\rangle_z(t) + \hat{\delta}_1^{\rm TR,BR}(z;t),\end{aligned} \tag{3}$$

with

$$\langle\delta_1^{\rm TR,BR}\rangle_z(t) = \frac{1}{L_z}\int_0^{L_z}\delta_1^{\rm TR,BR}(z;t)\,dz. \tag{4}$$

Figure 13 contains space-time diagrams for $\hat{\delta}_1^{\rm TR}$ (panel b) and $\hat{\delta}_1^{\rm BR}$ (d) alongside corresponding time series of C_l and C_d (a) and of spanwise-averaged $\langle\delta_1^{\rm TR}\rangle_z$ and $\langle\delta_1^{\rm BR}\rangle_z$ (c), for the three-dimensional periodic solution

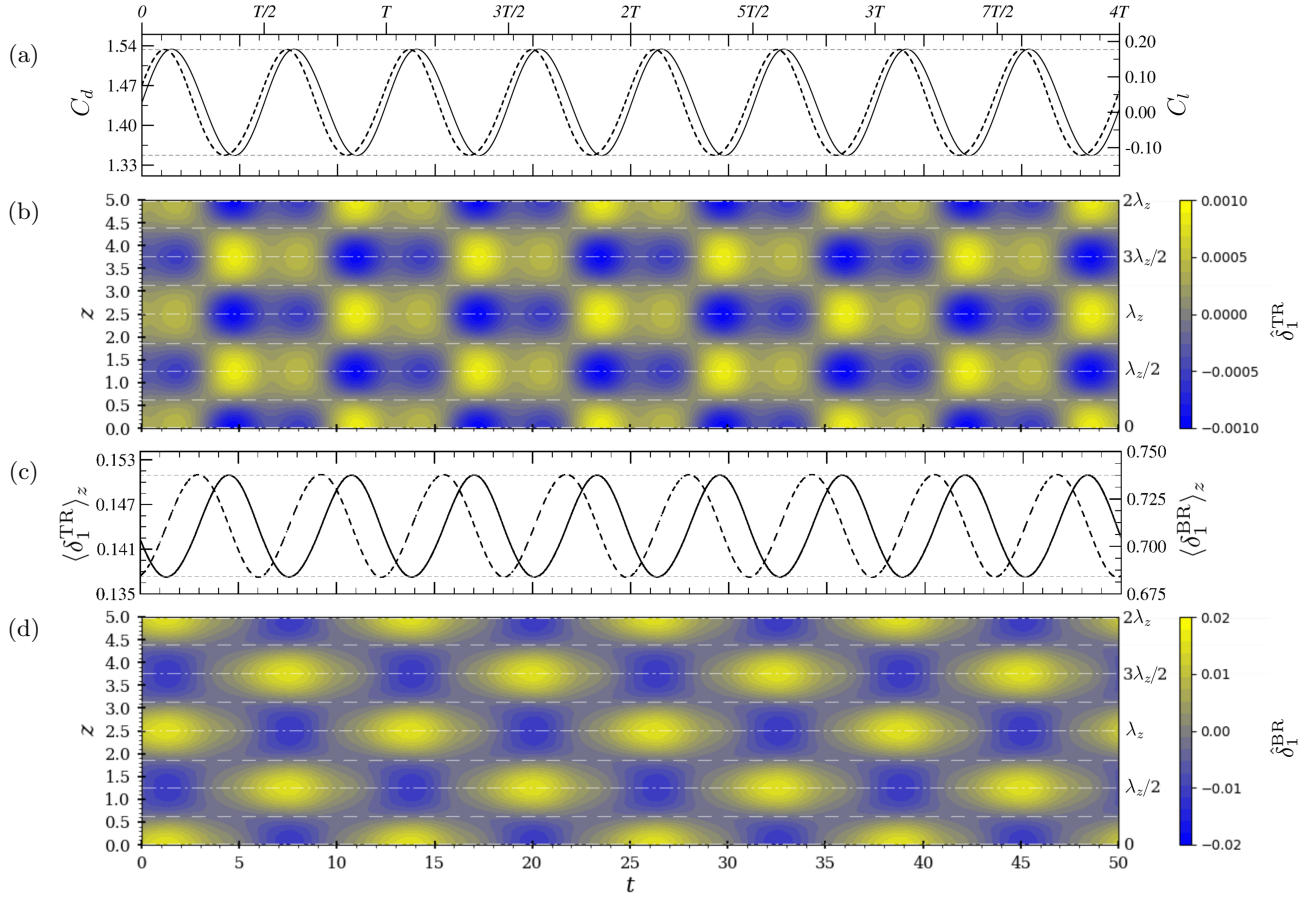

FIG. 13: Space-time properties of the $R = 3.4$ solution. Space-time diagrams for the spanwise modulation component of the displacement thickness at the trailing edge of the top $\hat{\delta}_1^{\mathrm{TR}}$ (b) and bottom $\hat{\delta}_1^{\mathrm{BR}}$ (d) cylinder walls. (a) Dynamic evolution of the lift C_l (solid) and drag C_d (dashed) coefficients. (c) Dynamic evolution of the spanwise-averaged component of the displacement thickness at the trailing edge of both the top $\langle\delta_1^{\mathrm{TR}}\rangle_z$ (solid) and bottom $\langle\delta_1^{\mathrm{BR}}\rangle_z$ (dashed) walls.

at $R = 3.4$. The space-time diagrams correspond to 8 complete vortex-shedding cycles, as clear from the C_l, C_d, $\langle\delta_1^{\mathrm{TR}}\rangle_z$ and $\langle\delta_1^{\mathrm{BR}}\rangle_z$ time series, and their periodicity follows exactly that of vortex shedding. The actual periodicity of the solution is however twice that of vortex shedding. The nature of the period doubling, which does not affect aggregate quantities, was thoroughly discussed by El Mansy et al. [66]. The only remaining symmetry once $R \neq 1$ has broken the top-bottom Z_2 symmetry, i.e. the spanwise invariance (involving arbitrary spanwise shifts, SO(2), and mirror reflections about all planes orthogonal to the spanwise direction, Z_2), is disrupted upon three-dimensionalisation of the flow, such that the continuous SO(2) turns into invariance with respect to discrete shifts by multiples of the wavelength λ_z, and the spanwise Z_2 reflection symmetry is only preserved at all times about planes located at $z = z_0 + (2j)\lambda_z/4$ (dash-dotted lines), where the origin for the spanwise coordinate has been chosen to enforce $z_0 = 0$, $\lambda_z = 2.5$ here and $j \in \mathbb{Z}$. Additionally, a space-time symmetry operation consisting in the evolution by half a period $T/2$, where T is the actual period of the solution corresponding to two vortex-shedding cycles, followed by reflection about any plane located at $z = z_0 + (2j + 1)\lambda_z/4$ (dashed lines), also leaves the solution invariant. The appropriate composition of the two symmetries shows that the solution is also invariant to evolution by half a period $T/2$, followed by a spanwise shift by a half wavelength $\lambda_z/2$.

As clear from figure 13a, the C_l (solid) and C_d (dashed) signals are nearly in phase, with the former trailing slightly behind the latter with a lag ($\Delta\phi \simeq \pi/9$). The spanwise-averaged top boundary layer thickness $\langle\delta_1^{\mathrm{TR}}\rangle_z$ (figure 13c, solid) evolves in phase opposition with aerodynamic forces, while the bottom boundary layer thickness $\langle\delta_1^{\mathrm{BR}}\rangle_z$ flaps with about four times the amplitude and roughly one-quarter-cycle phase advance ($\Delta\phi \simeq \pi/4$). The aerodynamic forces peak when the top boundary layer is at its thinnest and the bottom boundary layer growing fastest. The spanwise modulational component of the top and bottom boundary layers is illustrated by the space-time diagrams of figures 13b and d, respectively. The spanwise modulation amplitude is small for

the bottom boundary layer ($\sim 5.6\%$) and tiny for the top ($\sim 1.4\%$), and seems to be dictated by the spanwise average of the top boundary layer. As it happens, the modulation amplitude is highest for the top boundary layer when $\langle \delta_1^{\mathrm{TR}} \rangle_z$ is maximum, and highest for the bottom boundary layer when $\langle \delta_1^{\mathrm{TR}} \rangle_z$ is at its minimum. Three-dimensionality in the wake is therefore closest to the cylinder back when the top boundary layer has its maximum thickness, which indicates that the modulational instability develops on the top shear layer and is promoted when it is thicker.

At the slightly higher value $R = 3.8$, figure 14 shows how the aerodynamic force coefficients C_l and C_d (panel a), and $\langle \delta_1^{\mathrm{TR}} \rangle_z$ and $\langle \delta_1^{\mathrm{BR}} \rangle_z$ (panel c) time series have a period that is about twice that for $R = 3.4$. The period-doubling bifurcation is however of an altogether different nature. While aggregate quantities repeat every two vortex-shedding cycles, the solution at $R = 3.8$ is in fact period four. The space-time diagrams for $\hat{\delta}_1^{\mathrm{TR}}$ (b) and $\hat{\delta}_1^{\mathrm{BR}}$ (d) provide the full picture. As minutely reported by El Mansy et al. [66], the bifurcation that is responsible for the emergence of the period-doubled solution is spatially subharmonic, the spanwise wavelength doubling that of the solution at $R = 3.4$. This breaks the mirror symmetry and the only remaining symmetry leaves the solution invariant to evolution for half a period (two vortex-shedding cycles) followed by reflection about planes located at $z = z_0 + j\lambda_z/2$ (dashed lines), where now $\lambda_z = 5$. Everything discussed for $R = 3.4$ as to synchronicity of force coefficients and top and bottom boundary layer spanwise-averaged thickness holds for $R = 3.8$. C_d lags slightly behind C_l, and the top boundary layer is thickest and the bottom boundary layer grows fastest when C_d is at its lowest. The modulational amplitude of the top and bottom boundary layer thicknesses is however quite different from one vortex-shedding cycle to the next, and alternates two low peaks with one large peak. The largest modulational amplitude is synchronised between the top and bottom boundary layers and occurs once every two C_d valleys.

VI. CONCLUSIONS

We have analysed the aerodynamic performances and statistical wake topology of the flow past a square cylinder immersed in the near wake of a flat plate separating two homogeneous streams of different velocities. This flow configuration, though relevant to situations where structural struts or rods are placed in close proximity of upstream lift-producing devices, has rarely been considered in the literature. The Reynolds number associated to the bottom incoming stream Re_B has been kept fixed, such that changes in the top-to-bottom stream velocity ratio R modify simultaneously the bulk Reynolds number Re and a shear parameter K purposely defined in analogy to the homogeneous upstream shear case to characterise the incoming velocity difference across the cylinder height. Our results, though still incomplete, conclusively suggest that the parallel with the problem of bluff bodies in upstream shear broadly holds, and that most findings here can be related to the competing effects of Re and K there.

The recirculation bubble length l_r grows with R while the wake remains steady and recedes thereafter. This is the same trend reported for the classic square cylinder configuration upong increasing Re, the shear parameter playing no noticeable role[41]. Also, the vortex formation region l_f shrinks all along, analogously to what happens for the circular cylinder case. It would seem that the Re increase rather than that of K dictates the evolution of both. The drag coefficient C_d is pressure-dominated and increases with R, while the lift coefficient C_l is initially driven by friction on the front surface generating a net downforce, but later recovers into positive as pressure forces on the top and bottom surfaces take the lead. The slight initial decline of C_d follows from the paradoxical effects of increasing Re and K simultaneously. Both Re and K tend to reduce C_d at low $Re \lesssim 100$ and $K \lesssim 0.2$, but the trend is reversed thereafter[55,56] and C_d increases fast[41]. Meanwhile. the initial descent of C_l into negative values is driven by the increase of K at low Re[55,56], while the recovery that follows the advent of time dependence results from the concurrent effect of K and Re when both are sufficiently large[41,55,56].

The effect of the combined migration of the stagnation and base pressure points and the respective values of the pressure coefficient correlates well with the drag coefficient and, at the same time, satisfactorily explains the evolution of the boundary layer thickness distribution on the top and bottom surfaces as R is varied.

A close analysis of the downstream vortical structures as the flow evolves from steady to time-periodic, shows that just after the Hopf bifurcation vortex shedding consists already of a single vortical structure issued from the cylinder top rear corner, much as observed for homogeneous-shear incoming flow. The recirculation lobe on the lower mid wake simply expands and shrinks without ever separating from the cylinder. As the velocity ratio is increased, both the upper (negative) and lower (positive) lobes start detaching alternately, but vortices are only shed on the top half of the wake. The vorticity layer issued along the bottom-half of the wake does not roll up into forming vortices and quickly dissipates. The fact that the length of the vortex formation region is consistently shorter ($l_f^T < l_f^B$) and the normal Reynolds stress field $\langle u'u' \rangle$ peaks higher along the top shear layer than along the bottom, suggests that the former has a larger share in driving the wake instability.

The displacement thickness of the boundary layers developing on the top and bottom cylinder surfaces serve as an aerodynamic performance diagnosis tool and, at the same time, provide the means to relate the instantaneous evolution of the aerodynamic coefficients to the base pressure location and intensity. While the top boundary layer remains attached all along, the bottom boundary layer is

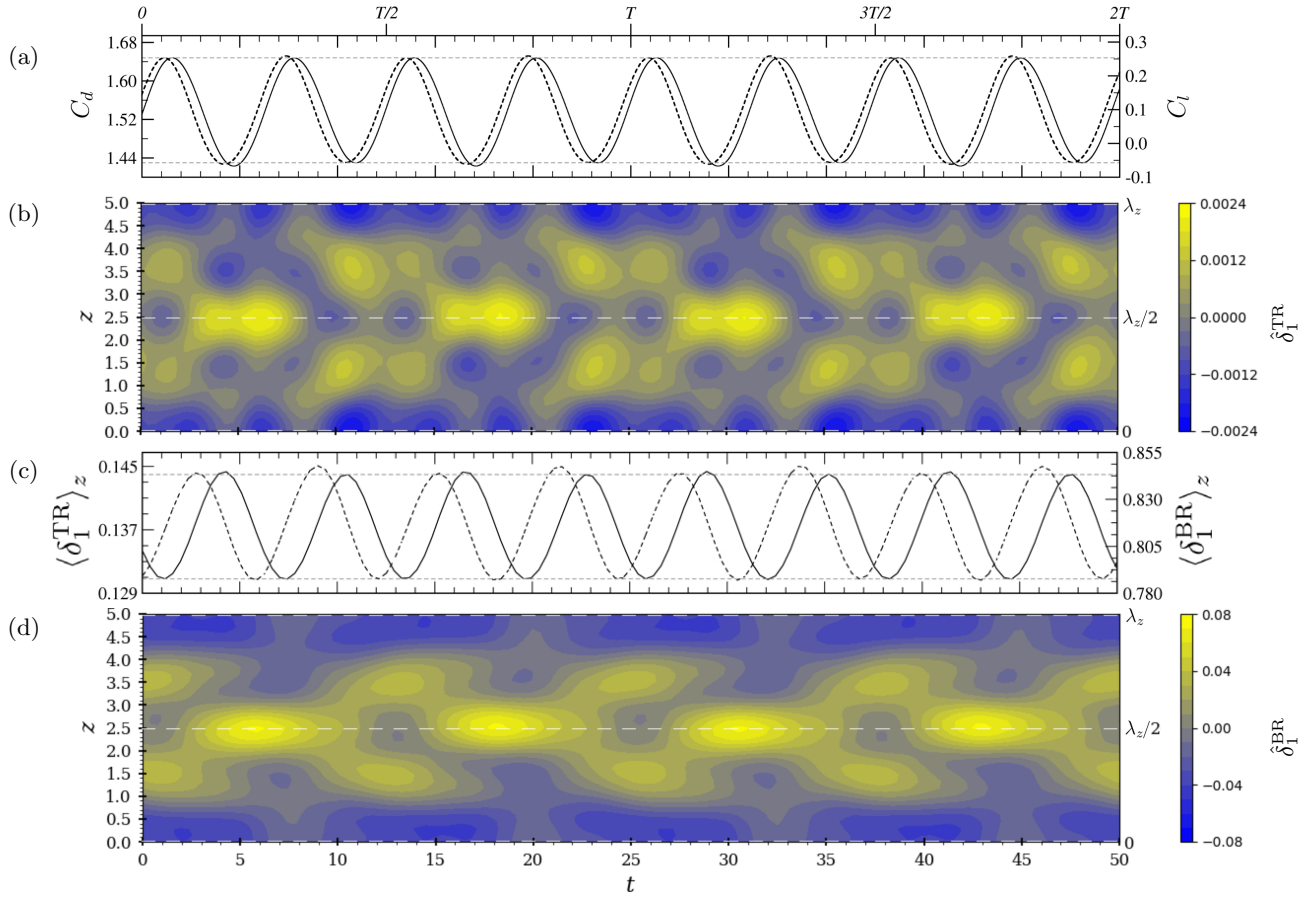

FIG. 14: Space-time properties of the $R = 3.8$ solution. Space-time diagrams for the spanwise modulation component of the displacement thickness at the trailing edge of the top $\hat{\delta}_1^{\mathrm{TR}}$ (b) and bottom $\hat{\delta}_1^{\mathrm{BR}}$ (d) cylinder walls. (a) Dynamic evolution of the lift C_l (solid) and drag C_d (dashed) coefficients. (c) Dynamic evolution of the spanwise-averaged component of the displacement thickness at the trailing edge of both the top $\langle\delta_1^{\mathrm{TR}}\rangle_z$ (solid) and bottom $\langle\delta_1^{\mathrm{BR}}\rangle_z$ (dashed) walls.

mostly detached although some reattachment occurs for large R during some phases of the vortex-shedding cycle. Attached or not, top and bottom boundary layers flap almost synchronously, in contrast to usual space-time symmetric Kármán vortex shedding, for which the flapping is in exact phase opposition. The lift force coefficient evolves with a small delay behind drag, and both are nearly in opposition of phase with respect to bottom and top boundary layer thicknesses, respectively. Minimum instantaneous C_d corresponds to highest base pressure, which results in a stronger adverse (or milder favourable) pressure gradient and thicker boundary layers along both the top and bottom surfaces. This maximum base pressure occurs precisely at the phase of vortex-shedding for which the base point is at its highest location. This contributes to boosting the pressure further on the top surface than on the bottom, which results in a downforce differential that brings C_l also to its minimum. Besides responding to aerodynamics performances in an intelligible way, boundary layer thicknesses help characterise the flow fields in terms of their spatio-temporal symmetries. The symmetries of the various solutions, which were minutely analysed by El Mansy et al. [66], are clearly imprinted in the time evolution of the spanswise distribution of the top and bottom boundary layers displacement thickness.

More detailed explorations in two-dimensional parameter space will be required in the future to decouple the independent effects of the bulk Reynolds number Re and the velocity ratio R. Besides, incoming velocity profiles other than homogeneous or linear (and this latter subject to the eventual subcritical instability of the Couette flow profile) are not self-sustained. The quasi-step profile intended here, although reproducible in actual experiments, is to some extent dependent on plate length and gap with the cylinder front face. A thorough parametric study would be required to assess the scope of validity of the result presented here. Such undertaking is underway and will be considered elsewhere.

ACKNOWLEDGEMENTS

This work was supported by the Spanish Government under grants FIS2016-77849-R and PID2020-114043GB-I00, and by the Catalan Government under grant 2017-SGR-00785. Part of the computations were done in the Red Española de Supercomputación (RES), Spanish supercomputing network, under grants FI-2019-1-0023 and FI-2018-3-0030. F. Mellibovsky is a Serra-Húnter fellow.

AUTHOR DECLARATIONS

The authors have no conflicts to disclose.

Appendix A: Method validation and domain size and grid resolution analyses

The spectral element space discretisation and the velocity correction time-stepping scheme used here for the flow past a square cylinder immersed in the wake of an upstream splitter plate separating two streams with different velocities have been validated against literature results using as benchmark the closely related problem of the flow past a stand-alone square cylinder in homogeneous flow at zero angle of attack and at comparable Reynolds numbers.

In the present study, the bottom stream Reynolds number has been kept fixed to $Re_B = 56$ throughout, while the top-to-bottom velocity ratio has been varied in the range $R \in [1, 5.357]$. The corresponding top stream Reynolds number is then $Re_T = RRe_B \leq 300$, and it would therefore make sense to use benchmark results for the classical square-cylinder-flow configuration at $Re = 300$ for mesh validation. The flow remains nevertheless two-dimensional for $R \lesssim 3.1$, so that the in-plane mesh for two-dimensional simulations might be safely based on comparison against two-dimensional square cylinder results anywhere below $Re \lesssim 175$.

The in-plane mesh has been designed according to the sketch shown in figure 15. The full domain has been partitioned in 10 subdomains for better local refinement of the structured quad mesh in critical regions such as close to the walls and along the wake. In particular, the near field (NF) and near wake (NW) regions have been singled out by devising a square around the cylinder of dimensions $h_{\rm MT} = h_{\rm MB} = l_{\rm UM} = l_{\rm DM} = 1.5$. The relation between domain partitioning and computational domain dimensions are $l_{\rm U} = L_x^u - l_{\rm UM}$, $l_{\rm D} = L_x^d - l_{\rm DM}$, $h_{\rm U} = h_{\rm D} = L_y/2 - h_{\rm MT} = L_y/2 - h_{\rm MB}$. The number of linear elements distributed along each one of the master sides of the various subdomain regions are $N_{\rm LU} = 22$, $N_{\rm LMT} = N_{\rm LMB} = N_{\rm HDM} = 49$, $N_{\rm LD} = 49$, $N_{\rm HT} = N_{\rm HB} = 29$, $N_{\rm HUM} = 46$ and $N_{\rm X} = 21$. The progression and bump features of gmesh have been used to ensure a maximum first cell layer thickness $d_w < 0.005$ and a growth rate below $k_w < 1.2$ away from the walls, including the splitter plate.

The stand-alone square cylinder at $Re = 150$, just short of entering the wake transition regime, has been selected as the benchmark for the design of the in-plane two-dimensional mesh described above for all two-dimensional cases. Aerodynamic performances aggregate quantites, collected over $T_{\rm stats} = 500$ advective time units (about 80 complete vortex-shedding cycles) after having let the solution evolve for $T_{\rm trans} = 600$ to overcome all transients, are presented in table I alongside literature results. Some details of the method (computational or experimental), domain dimensions, and space and time resolution and discretisation order are also provided for completeness. Our baseline combination of domain and mesh produces results in good agreement with a wide range of published data obtained using comparable numerical parameters. In particular, the downstream and cross-stream sizes of the domain, which follow the recommendations of Sohankar et al.[83,84] and Sharma and Eswaran[85], are clearly sufficient for accurate two-dimensional simulations at $Re = 150$. The vortex-shedding frequency (Strouhal number St) compares favourably with literature results, with deviations within 1% in most of the cases. The same goes for the mean drag coefficient C_d and the r.m.s. of the drag C_d' and lift C_l' coefficient signals, although published values spread over somewhat wider ranges. The maximum wall distance of the first layer of cells, measured in wall units ($y^+ \equiv yu_\tau/\nu$, with $u_\tau \equiv \sqrt{\tau_w/\rho}$ the friction velocity) resulted in $d_w^+ < 0.5$, well inside the viscous sublayer of an eventual turbulent boundary layer. Besides, it must be borne in mind that the actual d_w^+ is in fact half that value for a second order mesh and around 21.1% for a Lagrange polynomial expansion of order three due to the non equispaced distribution of the Gauss-Legendre collocation points. In combination with a very slow progression of cell thickness away from the wall $k_w < 1.2$, this is a good indication that boundary layers are well resolved.

In order to verify mesh resolution, we have increased the spectral element order, originally employing second order polynomial expansions, to three. The results, also presented in table I, quantify the degree to which the solution is grid-independent. All St, C_d, C_d' and C_l' parameters are accurate well within 1%. Downstream boundary location and blockage effects have also been assessed by doubling the downstream length of the domain to $L_z^d = 51$ (and increasing to $N_{\rm LD} = 68$) and by doubling the cross-stream height to $L_y = 32$ ($N_{\rm HT} = N_{\rm HB} = 33$). Doubling L_z^d produced no noticeable alteration of any of the aerodynamic performances indicators considered, while doubling L_y resulted in deviations well under 1%.

Since the flow remains two-dimensional up to $R = 3.1$, corresponding to $Re_T \simeq 175$, it is advisable to validate the method, domain and mesh against two-dimensional simulations past a square cylinder at the somewhat larger $Re = 200$. The results are given in table II. While St aligns still well with reported values in the literature, the

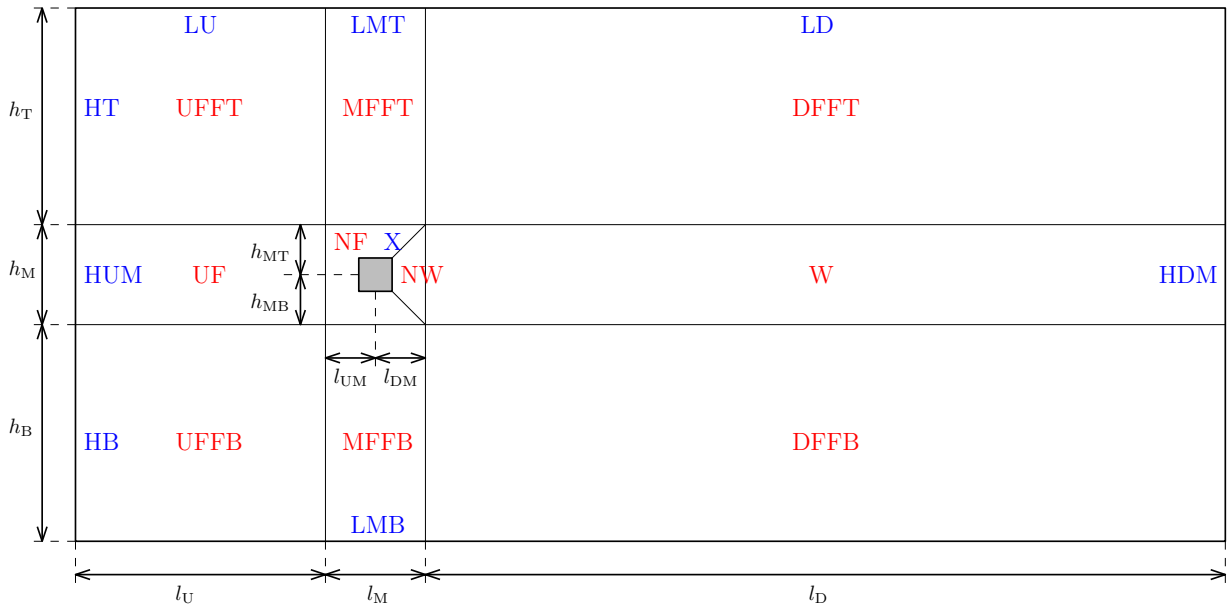

FIG. 15: Domain partitioning. The acronyms are as follows: U for upstream, D for downstream, N for near, F for field, FF for far field, T for top, B for bottom, M for mid, W for wake and X for wall-normal. Red text denotes subdomain regions, blue subdomain sides.

$Re = 150$	Method	L_x^u	L_x^d	L_y	L_z	$N_x \times N_y$	N_p	d_w	N_z	Δt	St	C_d	C_d'	C_l'
Baseline	SEM	9	25.5	16	-	120×107^2	193	0.0045	-	0.0018^2	0.160	1.510	0.0163	0.300
3rd order	SEM	9	25.5	16	-	120×107^3	193	0.0045	-	0.0008^2	0.160	1.505	0.0162	0.299
Double downstream	SEM	9	51	16	-	139×107^2	193	0.0045	-	0.0018^2	0.160	1.510	0.0163	0.300
Double cross-stream	SEM	9	25.5	32	-	120×115^2	193	0.0045	-	0.0018^2	0.159	1.497	0.0163	0.300
Sen et al. [75]	FEM	80	100	100	-	157108^1	664	0.005	-	0.03^2	0.159	1.508	0.017	0.303
Singh et al. [76]	FVM	8.5	24.5^C	18	-	250×150^2	320	0.007	-	0.01^2	0.159	1.516	-	0.287
Sharma and Eswaran [21]	FVM	9	17^C	20	-	323×264^3	-	0.01	-	0.001^1	0.160	1.465	0.0157	0.292
Wang et al. [77]	???	10.5	30.5	20	-	$??\times??^?$	-	?????	-	$?????^?$	0.160	1.474	-	0.285
Ali et al. [78]	FVM	10	20^C	20	-	520×440^3	400	0.01	-	0.005^1	0.160	1.470	-	0.285
Alam et al. [32]	FVM	11.5	38.5	20	-	112000^2	320	0.01	-	0.017^2	0.155	1.492	0.0155	0.272
	FVM	11.5	38.5	20	-	77000^2	320	0.01	-	0.015^2	0.155	1.493	0.0157	0.277
Zheng and Alam [79]	FVM	13.5	29.5	19	-	450964^2	280	0.0033	-	0.0024^2	0.159	1.476	0.0163	0.273
	FVM	13.5	29.5	27	-	154650^2	280	0.0033	-	0.0097^2	0.157	1.468	0.0165	0.275
Saha et al. [69]	FDM	6	18^C	10	-	178×80^2	-	-	-	0.015^2	0.163	1.541	0.017	0.274
Mashhadi et al. [16]	FVM	9.5	20.5	18	-	288×189^2	124	0.01	-	0.01^2	0.162	1.466	0.0136	0.269
Zhang et al. [80]	SEM	6	23	18	-	36×51^5	-	-	-	0.00293^2	0.163	1.558	-	-
Doolan [81]	FVM	10	20	20	-	250×180^2	-	0.0167	-	$0.0025^?$	0.156	1.44	-	0.293
Sohankar et al. [20]	FVM	8.5	12.5^C	18	-	169×121^2	100	0.004	-	0.025^2	0.165	1.44	-	0.23
Jiang and Cheng [15]	FVM	30	30	60	15	43922^2	196	0.005	120^2	0.015^2	0.155	1.417	-	0.269
Franke et al. [82]	FVM	5	15	12	-	88×76^3	-	0.0038	-	0.025^1	0.165	1.56	-	0.269^*
Okajima [19]	Exp				37.5	Water tank, towing type					0.139-44	1.4	-	-
Luo et al. [28]	Exp	$Tu < 0.35\%$			225	Wind tunnel, open-loop					0.16	-	-	-
Luo et al. [26]	Exp	$Tu \sim 1\%$			54	Water channel, recirculating					0.163	-	-	-

TABLE I: Validation against benchmark data and domain and grid independence study for the flow past a stand-alone square cylinder at $Re = 150$. Listed are the methods used (FDM: Finite Differences Method; FVM: Finite Volumes Method; FEM: Finite Elements Method; SEM: Spectral Elements Method; Exp: experimental), domain dimensions (the C superscript for L_x^d indicates that convective-type conditions are applied to the outlet boundary), mesh resolution (Superscripts denote order of the discretisation method -F for Fourier-, N_p indicates the number of divisions over the full cylinder perimeter, and d_w is the first cell layer thickness away from the walls), and a bunch of aerodynamic performance parameters (a star superscript in rms values indicates approximate estimation from time-series oscillation amplitude).

$Re = 200$ (2D)	Method	L_x^u	L_x^d	L_y	L_z	$N_x \times N_y$	N_p	d_w	N_z	Δt	St	C_d	C'_d	C'_l
Baseline	SEM	9	25.5	16	-	120×107^2	193	0.0045	-	0.0018^2	0.153	1.541	0.0338	0.488
3rd order	SEM	9	25.5	16	-	120×107^3	193	0.0045	-	0.0006^2	0.153	1.535	0.0333	0.485
Double downstream	SEM	9	51	16	-	139×107^2	193	0.0045	-	0.0018^2	0.153	1.541	0.0338	0.488
Double cross-stream	SEM	9	25.5	32	-	120×115^2	193	0.0045	-	0.0018^2	0.152	1.537	0.0336	0.485
Zhang et al. [80]	SEM	6	23	18	-	44×66^5	-	-	-	0.00195^2	0.155	1.583	0.0355	0.488
Franke et al. [82]	FVM	5	15	12	-	88×76^3	-	0.0013	-	0.025^1	0.157	1.60	-	0.438*
Mashhadi et al. [16]	FVM	9.5	20.5	18	-	288×189^2	124	0.01	-	0.01^2	0.156	1.480	0.0300	0.410
Sohankar et al. [84]	FVM	10	10^C	20	-	284×274^2	160	0.004	-	0.025^2	0.15	1.462	-	0.377
Sohankar et al. [83]	FVM	10	26	20	-	348×224^2	120	0.004	-	0.025^2	0.149	1.445	-	0.36
Sohankar et al. [20]	FVM	8.5	12.5^C	18	-	169×121^2	100	0.004	-	0.025^2	0.170	1.46	-	0.32
Saha et al. [69]	FDM	6	18^C	10	-	178×80^2	-	-	-	0.015^2	0.162	1.657	-	-
Davis and Moore [86]	FDM	5.5	10^C	12	-	51×62^2	44	-	-	0.05^2	0.165	1.710	-	-

TABLE II: Validation against benchmark data and domain and grid independence study for the two-dimensional flow past a stand-alone square cylinder at $Re = 200$. Columns and annotations as for table I.

spread of C_d and C'_l data is remarkable. We can however still claim fair agreement with a number of works by other authors.

Increasing the spatial discretisation order to three for the two-dimensional simulation at $Re = 200$ produced errors below 1% for all considered performance indicators except C'_d, which incurred a still fairly acceptable 1.5% deviation. As for $Re = 150$, two-dimensional computations at $Re = 200$ did not modify results upon doubling L_x^d, while deviations below 1% were obtained upon doubling $L_y/2$, the blockage effect tending to reduce as Re increases.

Finally, available three-dimensional data for the flow past a square cylinder at $Re = 200$ has been used to validate the method and our domain and mesh for three-dimensional computations. The data is provided in table III. We have used a periodic spanwise length $L_z = 10$, discretised with $N_z = 48$ Fourier modes, not quite sufficient to achieve the desirable standard of 6 orders of magnitude decay in modal energy but still sufficient to produce results that compare favourably with published data. St and C_d fall comfortably within ranges as reported in the literature. The same applies to C'_l, while our C'_d results appear rather small in comparison to the few studies that report them. In any case, C'_l and C'_d are known to be particularly prone to inaccuracies[83,84], especially across the wake transition regime, where force coefficients have been shown to incorporate a very small frequency modulation that requires extraordinarily long runs to collect meaningful averages and second moment statistics[20].

All results presented and discussed throughout this paper, two-dimensional and three-dimensional, have been extracted from computations based on the baseline domain and mesh described above, with Lagrange polynomial expansions of order two. The mesh was purposely refined in the cross-stream direction at the location where the splitter plate is placed. For three-dimensional computations, the periodic spanwise extent of the domain has been generally chosen so as to fit an integer number of times (commonly 2, sometimes 4) the most unstable wavelength as obtained from stability analysis of the underlying two-dimensional time-periodic solution. The spanwise resolution has been chosen in each case to ensure a modal energy decay of about 6 orders of magnitude from the largest non-zero spanwise mode.

It might however be argued that the presence of the splitter plate and the introduction of a top-bottom asymmetry through the prescription of different inlet velocities above and below the plate undermines the validity of the domain size and grid convergence studies discussed above. The cross-stream blockage and the location of the downstream boundary may indeed play a different role when the cylinder is subject to inhomogeneous incoming flow, as could also the mesh topology and local properties. In order to assess these effects in a situation that is meaningful to the flow configuration adressed in this study, a bunch of tests has been run for a steady ($R = 2$), a two-dimensional periodic ($R = 3$), and a three-dimensional solution ($R = 3.4$). Results are summarised in table IV. Doubling the downstream extent of the domain does not have a significant impact on results at any of the three values of R checked. The blockage efects are contained concerning St and C_d (less than 2%), and also C_l for $R = 2$ (3%). The $R = 3$ and $R = 3.4$ cases, however, show rather large deviations in C_l in relative terms, but the absolute deviation is in fact rather small. Relative errors are misleadingly large because lift is small and indeed vanishes somewhere in between the two regimes. Force coefficient fluctuation deviations seem to peak in the late two-dimensional vortex-shedding regime, with deviations of around 10% with respect to baseline. It appears, however, that the advent of three-dimensionality effectively downplays blockage effects, with C'_d and C'_l again within acceptable 2.5% and 1.5%, respectively. Doubling the spanwise extent of the domain for the three-dimensional solution at $R = 3.4$ does not modify the performance monitors, as the solution preserves the exact same spanwise wavelength and simply fits twice in the domain instead of just once. Fi-

$Re = 200$ (3D)	Method	L_x^u	L_x^d	L_y	L_z	$N_x \times N_y$	N_p	d_w	N_z	Δt	St	C_d	C_d'	C_l'
Baseline	SEM	9	25.5	16	10	120×107^2	193	0.0045	48^F	0.0018^2	0.154	1.495	0.0180	0.289
Mahir [70]	FDM	7.5	20^C	15	6	177×127^2	-	0.01	25^2	0.01^2	0.154	1.518	-	0.305
Mashhadi et al. [16]	FVM	9.5	20.5	18	7	288×189^2	204	0.01	70^2	0.01^2	0.151	1.440	0.0258	0.320
Saha et al. [69]	FDM	6	18^C	10	10	178×80^2	-	-	22^2	0.015^2	0.161	1.600	0.026	0.305
Visakh et al. [87]	FDM	7.5	20^C	20	6	274×200^2	-	0.005	30^2	$?^2$	0.158	1.43	0.026	0.29
Sohankar et al. [20]	FVM	8.5	12.5^C	18	10	169×121^2	100	0.004	41^2	0.025^2	0.160	1.41	-	0.22
	FVM	8.5	12.5^C	18	6	169×121^2	100	0.004	25^2	0.025^2	0.157	1.39	-	0.21
Jiang and Cheng [15]	FVM	30	30	60	15	43922^2	196	0.005	120^2	0.015^2	0.149	1.394	-	0.25
Okajima [19]	Exp				37.5	Water tank, towing type					0.148-55	1.4	-	-
Luo et al. [28]	Exp	$Tu < 0.35\%$			225	Wind tunnel, open-loop					0.159	-	-	-
Luo et al. [26]	Exp	$Tu \sim 1\%$			54	Water channel, recirculating					0.160	-	-	-

TABLE III: Validation against benchmark data and domain and grid independence study for three-dimensional flow past a stand-alone square cylinder at $Re = 200$. Columns and annotations as for table I.

Case	Test	St	C_d	C_d'	C_l	C_l'
$R = 2$ (Steady)	Baseline	0	0.972	0	-0.1087	0
	Third order	0	0.969	0	-0.1100	0
	Double downstream	0	0.989	0	-0.1107	0
	Double cross-stream	0	0.974	0	-0.1055	0
$R = 3$ (2D periodic)	Baseline	0.155	1.245	0.0336	-0.0450	0.0589
	Third order	0.155	1.258	0.0336	-0.0445	0.0597
	Double downstream	0.156	1.244	0.0336	-0.0450	0.0588
	Double cross-stream	0.155	1.224	0.0308	-0.0374	0.0533
$R = 3.4$ (3D periodic)	Baseline ($L_z = 2.5$)	0.160	1.436	0.0658	0.0279	0.1065
	Third order	0.159	1.444	0.0656	0.0310	0.1055
	Double spanwise	0.160	1.436	0.0658	0.0287	0.1065
	Double downstream	0.160	1.436	0.0659	0.0279	0.1066
	Double cross-stream	0.160	1.414	0.0643	0.0241	0.1081

TABLE IV: Domain and mesh validation tests for the flow past a square cylinder immersed in the interface of two different-velocity streams.

nally, increasing the polynomial expansions order to three kept deviations of all parameters below 1% except for C_l at $R = 3.4$, again due to the deceitful artifact of comparing relative errors for a vanishing quantity.

Although not specifically shown here, the bifurcation sequence, solution types and flow fields were not qualitatively affected by either increasing resolution or domain dimensions from baseline. In particular, stagnation, base, separation and reattachment points location on the cylinder surface, wake topology and vortex shedding characteristics where indistinguishable to the naked eye.

Appendix B: Aerodynamic performances and peak Reynolds stresses

The aerodynamic performances data that has been used in producing figures 2 and 6 is given in table V for completeness. Peak values and location of the Reynolds stresses are presented in table VI.

[1] M. Kiya, H. Tamura, and M. Arie. Vortex shedding from a circular cylinder in moderate-Reynolds-number shear flow. *J. Fluid Mech.*, 101(4):721–735, 1980.

[2] H. Tamura, M. Kiya, and M. Arie. Numerical study on viscous shear flow past a circular cylinder. *Bulletin of JSME*, 23(186): 1952–1958, 1980.

[3] T.S. Kwon, H.J. Sung, and J.M. Hyun. Experimental investigation of uniform-shear flow past a circular cylinder. *J. Fluid Eng-T. Asme.*, pages 457–460, 1992.

[4] K. Ayukawa, J. Ochi, G. Kawahara, and T. Hirao. Effects of shear rate on the flow around a square cylinder in a uniform shear flow. *J. Wind Eng. Ind. Aerod.*, 50:97–106, 1993.

[5] R.R. Hwang and Y.C. Sue. Numerical simulation of shear effect on vortex shedding behind a square cylinder. *Int. J. Numer. Meth. Fl.*, 25(12):1409–1420, 1997.

[6] H.J. Zhang, L. Huang, and Y. Zhou. Aerodynamic loading on a cylinder behind an airfoil. *Experiments in fluids*, 38(5):588–593, 2005.

[7] X.F. Niu, Y. Li, and X.N. Wang. Numerical study of aerodynamic noise behaviors for a vertically-installed flat strut behind an asymmetrical airfoil. *European Journal of Mechanics-B/Fluids*, 88:17–33, 2021.

[8] D. Rockwell. Vortex-body interactions. *Annu. Rev. Fluid Mech.*, 30:199–229, 1998.

[9] J. N. Lefebvre and A.R. Jones. Experimental investigation of airfoil performance in the wake of a circular cylinder. *AIAA J.*, 57(7):2808–2818, 2019.

[10] Z. Zhang, Z. Wang, and I. Gursul. Lift enhancement of a stationary wing in a wake. *AIAA J.*, 58(11):4613–4619, 2020.

[11] X. Shan. Effect of an upstream cylinder on the wake dynamics of two tandem cylinders with different diameters at low Reynolds numbers. *Phys. Fluids*, 33(8), 2021.

R	f	$\langle C_d \rangle$	C'_d	$\langle C_l \rangle$	C'_l	$\langle y_s \rangle$	y'_s	$\langle y_b \rangle$	y'_b	$\langle C_p^s \rangle$	$\langle C_p^b \rangle$
1.0	0	0.915	0	0	0	0	0	0	0	0.272	-0.384
1.2	0	0.897	0	-0.037	0	0.267	0	-0.034	0	0.349	-0.377
1.4	0	0.902	0	-0.066	0	0.336	0	-0.061	0	0.480	-0.369
1.6	0	0.920	0	-0.088	0	0.364	0	-0.085	0	0.628	-0.362
1.8	0	0.954	0	-0.105	0	0.378	0	-0.106	0	0.780	-0.354
2.0	0	0.972	0	-0.109	0	0.385	0	-0.109	0	0.929	-0.346
2.2	0.134	1.003	0.0005	-0.115	0.0012	0.388	0.0001	-0.152	0.004	1.057	-0.357
2.4	0.140	1.059	0.0038	-0.108	0.0083	0.388	0.0002	-0.169	0.028	1.197	-0.369
2.6	0.146	1.113	0.0083	-0.091	0.0166	0.388	0.0005	-0.184	0.055	1.320	-0.384
2.8	0.150	1.174	0.0170	-0.065	0.0311	0.387	0.0008	-0.195	0.093	1.434	-0.405
3.0	0.155	1.245	0.0336	-0.045	0.0589	0.385	0.0014	-0.169	0.141	1.546	-0.430
3.1	0.157	1.284	0.0446	-0.037	0.0754	0.385	0.0018	-0.133	0.173	1.604	-0.440
3.4	0.160	1.436	0.0658	0.029	0.1065	0.379	0.0024	-0.117	0.182	1.832	-0.466
3.8	0.161	1.533	0.0784	0.094	0.1121	0.376	0.0022	-0.097	0.192	1.999	-0.491
4.0	0.163	1.571	0.0811	0.127	0.1085	0.373	0.0018	-0.064	0.195	2.110	-0.527
5.357	0.160	1.827	0.0719	0.269	0.0837	0.362	0.0021	-0.021	0.134	2.598	-0.545

TABLE V: Aerodynamic performances data at the various values of R explored in the paper.

R	$\langle u'u' \rangle_{\max}$	$\mathbf{r}_2^{\langle u'u' \rangle}$	$\langle v'v' \rangle_{\max}$	$\mathbf{r}_2^{\langle v'v' \rangle}$	$\langle u'v' \rangle_{\max}$	$\mathbf{r}_2^{\langle u'v' \rangle}$	$\langle w'w' \rangle_{\max}$	$\mathbf{r}_2^{\langle w'w' \rangle}$
2.2	0.015	$(18.76, 0.60)$	0.053	$(22.9, 0.36)$	-0.017	$(16.57, 0.59)$	-	-
2.4	0.041	$(7.60, 0.62)$	0.109	$(13.6, 0.41)$	-0.041	$(8.98, 0.54)$	-	-
2.6	0.057	$(5.96, 0.60)$	0.142	$(11.1, 0.37)$	-0.053	$(7.09, 0.51)$	-	-
2.8	0.075	$(5.01, 0.58)$	0.175	$(9.1, 0.37)$	-0.067	$(5.79, 0.51)$	-	-
3.0	0.096	$(3.90, 0.57)$	0.213	$(7.6, 0.36)$	-0.083	$(4.88, 0.55)$	-	-
3.1	0.106	$(3.50, 0.56)$	0.232	$(6.9, 0.36)$	-0.093	$(4.28, 0.46)$	-	-
3.4	0.125	$(3.03, 0.58)$	0.270	$(6.2, 0.32)$	-0.109	$(3.86, 0.44)$	0.005	$(2.72, -0.25)$
3.8	0.137	$(2.88, 0.56)$	0.292	$(6.0, 0.31)$	-0.127	$(3.71, 0.42)$	0.013	$(2.69, -0.29)$
4.0	0.145	$(2.92, 0.55)$	0.293	$(5.5, 0.29)$	-0.126	$(3.67, 0.41)$	0.030	$(8.24, -0.47)$
5.357	0.169	$(3.00, 0.51)$	0.357	$(4.2, 0.12)$	-0.154	$(3.74, 0.36)$	0.041	$(3.28, -0.31)$

TABLE VI: Peak values of the Reynolds stresses and location as a function of R.

[12] Z. Zhang, Z. Wang, and I Gursul. Aerodynamics of a wing in turbulent bluff body wakes. *J. Fluid Mech.*, 937, 2022.

[13] T. Igarashi. Characteristics of the flow around 2 circular-cylinders arranged in tandem .1. *Bulletin of JSME*, 24(188): 323–331, 1981.

[14] L. Wang, M.M. Alam, and Y. Zhou. Two tandem cylinders of different diameters in cross-flow: effect of an upstream cylinder on wake dynamics. *J. Fluid Mech.*, 836:5–42, 2018.

[15] H. Jiang and L. Cheng. Hydrodynamic characteristics of flow past a square cylinder at moderate Reynolds numbers. *Phys. Fluids*, 30(10), 2018.

[16] A. Mashhadi, A. Sohankar, and M.M. Alam. Flow over rectangular cylinder: Effects of cylinder aspect ratio and Reynolds number. *Int. J. Mech. Sci.*, 195, 2021.

[17] D.H. Yoon, K.S. Yang, and C.B. Choi. Flow past a square cylinder with an angle of incidence. *Phys. Fluids*, 22(4):043603, 2010.

[18] H. Bai and M.M. Alam. Dependence of square cylinder wake on Reynolds number. *Phys. Fluids*, 30(1):015102, 2018.

[19] A. Okajima. Strouhal numbers of rectangular cylinders. *J. Fluid Mech.*, 123:379–398, 1982.

[20] A. Sohankar, C. Norberg, and L. Davidson. Simulation of three-dimensional flow around a square cylinder at moderate Reynolds numbers. *Phys. Fluids*, 11(2):288–306, 1999.

[21] A. Sharma and V. Eswaran. Heat and fluid flow across a square cylinder in the two-dimensional laminar flow regime. *Numer. Heat Tranf. Part A.*, 45(3):247–269, 2004.

[22] A. Roshko. On the development of turbulent wakes from vortex streets. Technical Report TR 1191, California Institute of Technology, 1954.

[23] J. H. Gerrard. The mechanics of the formation region of vortices behind bluff bodies. *J. Fluid Mech.*, 25(2):401–413, 1966.

[24] J.H. Gerrard. The wakes of cylindrical bluff bodies at low Reynolds number. *Phil. Trans. Roy. Soc. Lond. A*, 288(1354): 351–382, 1978.

[25] C. Norberg. LDV-measurements in the near wake of a circular cylinder. *ASME*, pages 41–5, 1998.

[26] S.C. Luo, X.H. Tong, and B.C. Khoo. Transition phenomena in the wake of a square cylinder. *J. Fluid. Struct.*, 23(2):227–248, 2007.

[27] X.H. Tong, S.C. Luo, and B.C. Khoo. Transition phenomena in the wake of an inclined square cylinder. *J. Fluid. Struct.*, 24(7): 994–1005, 2008.

[28] S.C. Luo, Y.T. Chew, and Y.T. Ng. Characteristics of square cylinder wake transition flows. *Phys. Fluids*, 15(9):2549–2559, 2003.

[29] H. Jiang, L. Cheng, and H. An. Three-dimensional wake transition of a square cylinder. *J. Fluid Mech.*, 842:102–127, 2018.

[30] C. Norberg. Effects of Reynolds number and a low-intensity freestream turbulence on the flow around a circular cylinder. Technical Report 87/2, Chalmers University, Göteborg, Sweden,

1987.
[31]H. Jiang and L. Cheng. Flow separation around a square cylinder at low to moderate Reynolds numbers. *Phys. Fluids*, 32(4): 044103, 2020.
[32]M.M Alam, T. Abdelhamid, and A. Sohankar. Effect of cylinder corner radius and attack angle on heat transfer and flow topology. *Int. J. Mech. Sci.*, 175, 2020.
[33]S.K. Jordan and J.E. Fromm. Laminar flow past a circle in a shear flow. *Phys. Fluids*, 15(6):972–976, 1972.
[34]H.J. Sung, C.K. Chun, and J.M. Hyun. Experimental study of uniform-shear flow past a rotating cylinder. *J. Fluid Eng-T. Asme.*, pages 62–67, 1995.
[35]T. Wu and C.F. Chen. Laminar boundary-layer separation over a circular cylinder in uniform shear flow. *Acta Mech.*, 144(1): 71–82, 2000.
[36]C. Lei, L. Cheng, and K. Kavanagh. A finite difference solution of the shear flow over a circular cylinder. *Ocean Eng.*, 27(3): 271–290, 2000.
[37]D. Sumner and O.O. Akosile. On uniform planar shear flow around a circular cylinder at subcritical Reynolds number. *J. Fluid. Struct.*, 18(3-4):441–454, sep 2003.
[38]S. Kang. Uniform-shear flow over a circular cylinder at low Reynolds numbers. *J. Fluid. Struct.*, 22(4):541–555, 2006.
[39]S. Cao, S. Ozono, K. Hirano, and Y. Tamura. Vortex shedding and aerodynamic forces on a circular cylinder in linear shear flow at subcritical Reynolds number. *J. Fluid. Struct.*, 23(5):703–714, 2007.
[40]S. Cao, S. Ozono, Y. Tamura, Y.J. Ge, and H. Kikugawa. Numerical simulation of Reynolds number effects on velocity shear flow around a circular cylinder. *J. Fluid. Struct.*, 26(5):685–702, 2010.
[41]A. Lankadasu and S. Vengadesan. Shear effect on square cylinder wake transition characteristics. *Int. J. Numer. Meth. Fl.*, 67(9): 1115–1134, 2011.
[42]S. Cao, Q. Zhou, and Z. Zhou. Velocity shear flow over rectangular cylinders with different side ratios. *Comput. Fluids*, 96: 35–46, 2014.
[43]T. Adachi. Study on the flow about a circular cylinder in shear flow. *Trans. Jpn. Soc. Aeronaut. Space Sci.*, 256:45–53, 1975.
[44]T. Hayashi, F. Yoshino, and R. Waka. The aerodynamic characteristics of a circular cylinder with tangential blowing in uniform shear flows. *JSME Int. J. Ser. B.*, 36(1):101–112, 1993.
[45]F. Yoshino and T. Hayashi. The numerical solution of flow around a rotating circular cylinder in uniform shear flow. *Bulletin of JSME*, 27(231):1850–1857, 1984.
[46]S. Cao and Y. Tamura. Flow around a circular cylinder in linear shear flows at subcritical Reynolds number. *J. Wind Eng. Ind. Aerod.*, 96(10-11):1961–1973, 2008.
[47]T. Hayashi. On the evaluation of the aerodynamic forces acting on a circular cylinder in a uniform shear flow. *Trans. Jpn. Soc. Mech. C.*, 56:31–36, 1990.
[48]M. Cheng, S.H.N. Tan, and K.C. Hung. Linear shear flow over a square cylinder at low Reynolds number. *Phys. Fluids*, 17(7): 078103, 2005.
[49]M. Cheng, D.S. Whyte, and J. Lou. Numerical simulation of flow around a square cylinder in uniform-shear flow. *J. Fluid. Struct.*, 23(2):207–226, 2007.
[50]S. Gsell, R. Bourguet, and M. Braza. Vortex-induced vibrations of a cylinder in planar shear flow. *J. Fluid Mech.*, 825:353–384, 2017.
[51]A. Kumar and R.K. Ray. Structural bifurcation analysis of vortex shedding from shear flow past circular cylinder. *Comput. Appl. Math.*, 38(3):1–25, 2019.
[52]A. Kumar and R.K. Ray. Numerical study of shear flow past a square cylinder at Reynolds numbers 100, 200. *Procedia Engineering*, 127:102–109, 2015.
[53]R.K. Ray and A. Kumar. Numerical study of shear rate effect on unsteady flow separation from the surface of the square cylinder using structural bifurcation analysis. *Phys. Fluids*, 29(8):083604, 2017.
[54]A.K. Saha, G. Biswas, and K. Muralidhar. Influence of inlet shear on structure of wake behind a square cylinder. *J. Eng. Mech.*, 125(3):359–363, 1999.
[55]S. Cao, Y. Ge, and Y. Tamura. Shear effects on flow past a square cylinder at moderate Reynolds numbers. *J. Eng. Mech.*, 138(1):116–123, 2012.
[56]A. Sohankar, E. Rangraz, M. Khodadadi, and M.M. Alam. Fluid flow and heat transfer around single and tandem square cylinders subjected to shear flow. *J. Braz. Soc. Mech. Sci.*, 42(8):1–22, 2020.
[57]G.J. Sheard, M.C Thompson, and K. Hourigan. From spheres to circular cylinders: the stability and flow structures of bluff ring wakes. *J. Fluid Mech.*, 492:147–180, 2003.
[58]G.J. Sheard, M.J. Fitzgerald, and K. Ryan. Cylinders with square cross-section: wake instabilities with incidence angle variation. *J. Fluid Mech.*, 630:43–69, 2009.
[59]D. Park and K.S. Yang. Effects of planar shear on the three-dimensional instability in flow past a circular cylinder. *Phys. Fluids*, 30(3):034103, 2018.
[60]A. Mushyam and J.M. Bergada. A numerical investigation of wake and mixing layer interactions of flow past a square cylinder. *Mec*, 52(1):107–123, 2017.
[61]B. An, J.M. Bergadà, F. Mellibovsky, W.M. Sang, and C. Xi. Numerical investigation on the flow around a square cylinder with an upstream splitter plate at low Reynolds numbers. *Meccanica*, pages 1–23, 2020.
[62]R.B. Loucks and J.M. Wallace. Velocity and velocity gradient based properties of a turbulent plane mixing layer. *J. Fluid Mech.*, 699:280, 2012.
[63]M.M. Rogers and R.D. Moser. The three-dimensional evolution of a plane mixing layer: the Kelvin–Helmholtz rollup. *J. Fluid Mech.*, 243(-1):183, oct 1992.
[64]R.D. Moser and M.M Rogers. The three-dimensional evolution of a plane mixing layer: pairing and transition to turbulence. *J. Fluid Mech.*, 247:275–320, 1993.
[65]R.D. Moser and M.M. Rogers. Mixing transition and the cascade to small scales in a plane mixing layer. *Phys. Fluids A-Fluid*, 3 (5):1128–1134, may 1991.
[66]R. El Mansy, W. Sarwar, J.M. Bergada, and F. Mellibovsky. Square cylinder in the interface of two different-velocity streams, 2022. URL `https://arxiv.org/abs/2202.01053`.
[67]C.D. Cantwell, D. Moxey, A. Comerford, A. Bolis, G. Rocco, G. Mengaldo, D. De Grazia, S. Yakovlev, J.E. Lombard, D. Ekelschot, et al. Nektar++: An open-source spectral/hp element framework. *Comput. Phys. Commun.*, 192:205–219, 2015.
[68]David Moxey, Chris D Cantwell, Yan Bao, Andrea Cassinelli, Giacomo Castiglioni, Sehun Chun, Emilia Juda, Ehsan Kazemi, Kilian Lackhove, Julian Marcon, et al. Nektar++: Enhancing the capability and application of high-fidelity spectral/hp element methods. *Comput. Phys. Commun.*, 249:107110, 2020.
[69]A.K. Saha, G. Biswas, and K. Muralidhar. Three-dimensional study of flow past a square cylinder at low Reynolds numbers. *Int. J. Heat Fluid Fl.*, 24(1):54–66, 2003.
[70]N. Mahir. Three dimensional heat transfer from a square cylinder at low Reynolds numbers. *Int. J. Therm. Sci.*, 119:37–50, 2017.
[71]A. Lankadasu and S. Vengadesan. Onset of vortex shedding in planar shear flow past a square cylinder. *Int. J. Heat Fluid Fl.*, 29(4):1054–1059, 2008.
[72]P.J. Strykowski and K.R. Sreenivasan. On the formation and suppression of vortex shedding at low Reynolds numbers. *J. Fluid Mech.*, 218:71–107, 1990.
[73]M.S. Bloor. The transition to turbulence in the wake of a circular cylinder. *J. Fluid Mech.*, 19(2):290–304, 1964.
[74]M.S. Bloor and J.H. Gerrard. Measurements on turbulent vortices in a cylinder wake. *Proc. Math. Phys. Eng. Sci.*, 294(1438): 319–342, 1966.
[75]S. Sen, S. Mittal, and G. Biswas. Flow past a square cylinder at low Reynolds numbers. *Int. J. Numer. Meth. Fl.*, 67(9):1160–1174, 2011.

[76] A.P. Singh, A.K. De, V.K. Carpenter, V. Eswaran, and K. Muralidhar. Flow past a transversely oscillating square cylinder in free stream at low Reynolds numbers. *Int. J. Numer. Meth. Fl.*, 61(6):658–682, 2009.

[77] J. Wang, Y. Xu, and H. Cheng. Features of flow past square cylinder with a perforated plate. *Trans. Tianjin Univ.*, 22(6): 544–554, 2016.

[78] M.S.M. Ali, C.J. Doolan, and V. Wheatley. Grid convergence study for a two-dimensional simulation of flow around a square cylinder at a low Reynolds number. In *Seventh International Conference on CFD in The Minerals and Process Industries (ed. PJ Witt & MP Schwarz)*, pages 1–6, 2009.

[79] Q. Zheng and M.M. Alam. Intrinsic features of flow past three square prisms in side-by-side arrangement. *J. Fluid Mech.*, 826: 996–1033, 2017.

[80] H. Zhang, D. Xin, J. Zhan, and L. Zhou. Flow past a transversely oscillating cylinder at lock-on region and three-dimensional Floquet stability analysis of its wake. *Phys. Fluids*, 33(2), 2021.

[81] C.J. Doolan. Flat-plate interaction with the near wake of a square cylinder. *AIAA J.*, 47(2):475–479, 2009.

[82] R. Franke, W. Rodi, and B. Schönung. Numerical calculation of laminar vortex-shedding flow past cylinders. *J. Wind Eng. Ind. Aerod.*, 35:237–257, 1990.

[83] A. Sohankar, C. Norbergb, and L. Davidson. Numerical simulation of unsteady low-Reynolds number flow around rectangular cylinders at incidence. *J. Wind Eng. Ind. Aerod.*, 69:189–201, 1997.

[84] A. Sohankar, C. Norberg, and L. Davidson. Low-Reynolds-number flow around a square cylinder at incidence: study of blockage, onset of vortex shedding and outlet boundary condition. *Int. J. Numer. Meth. Fl.*, 26(1):39–56, 1998.

[85] A. Sharma and V. Eswaran. Effect of channel confinement on the two-dimensional laminar flow and heat transfer across a square cylinder. *Numer. Heat Tranf. Part A.*, 47(1):79–107, 2005.

[86] R.W. Davis and E.F. Moore. A numerical study of vortex shedding from rectangles. *J. Fluid Mech.*, 116:475–506, 1982.

[87] M.G. Visakh, A.K. Saha, and K. Muralidhar. Effect of spanwise shear on flow past a square cylinder at intermediate Reynolds numbers. *Phys. Fluids*, 28(3), 2016.